Mnx1 Induces Leukemia Transformation Through Altering Histone Methylation in a Model of Pediatric t(7;12) Acute Myeloid Leukemia

Ahmed Waraky[1,2], Anders Östlund[1], Tina Nilsson[2], Dieter Weichenhan[4], Pavlo Lutsik[4], Marion Bähr[4], Joschka Hey[4], Jenni Adamsson[2], Mohammad Hamdy, Abdelrazak Morsy [3], Susann Li[2], Linda Fogelstrand[1,2], Christoph Plass[4] and Lars Palmqvist[1,2*]

[1]Department of Laboratory Medicine, Institute of Biomedicine, University of Gothenburg, and [2]Department of Clinical Chemistry, Sahlgrenska University Hospital, Gothenburg, Sweden.

[3]Department of laboratory medicine, division of Pathology, Karolinska institutet, Stockholm, Sweden.

[4]Division of Cancer Epigenomics, German Cancer Research Center (DKFZ), Heidelberg, Germany.

*Corresponding author

Lars Palmqvist MD, PhD

E-mail: lars.palmqvist@clinchem.gu.se

Institute of Biomedicine, University of Gothenburg

Sahlgrenska University Hospital,

SE-413 45 Gothenburg, Sweden

Phone: +46-31-3427829, Fax: +46-31-828458

SUMMARY

Acute myeloid leukemia (AML) in children with certain genetic aberrations is still associated with inferior outcome. One of these AML subtypes has a translocation t(7;12)(q36;p13) and in this study we have investigated the transforming event behind this AML and possible ways to target its effects. This translocation leads to a gene fusion MNX1::ETV6 but also to high ectopic expression of MNX1. However, only MNX1 was able to induce AML in a mouse model and this was only observed using hematopoietic stem and progenitor cells (HSPC) derived from fetal origin and not from adult bone marrow. This AML was highly penetrant in immunocompromised mice but only partly so in immunocompetent mice. The restriction in transforming capacity to cells from fetal liver origin is in concordance with the clinical finding that t(7;12)(q36;p13) AML is mostly restricted to infants. Molecularly, ectopic expression of MNX1 led to increased H3K4mono, di- and trimethylation and reduction in H3K27me3, both globally and on specific gene promoters. These alternations in histone methylation appeared to be mediated through MNX1 interaction with the methionine cycle and different methyl transferases. The alternations in histone methylation were accompanied with changes in genome wide chromatin accessibility as evident by ATAC-sequencing. We also found that high MNX1 expression resulted in increased DNA damage, which was accompanied by a depletion in the Lin-/Sca1+/c-Kit+ population and skewing toward myeloid lineage. These effects could be prevented by Sinefungin treatment of HSPC, which also halted leukemia development in mice. Comparison of gene expression profile of leukemia cells from our mouse AML model with human induced pluripotent stem cells with t(7;12) differentiated into HSPC showed similar pathway enrichment. In conclusion, we have shown the importance of MNX1 in leukemia development in the t(7;12) AML subtype and the rationale for targeting MNX1 and its downstream pathways.

INTRODUCTION

Non-random cytogenetic aberrations are often involved in the development of Acute myeloid leukemia (AML) and several aberrations can serve as diagnostic markers, prognosis predictors and impact choice of therapy (Lagunas-Rangel et al., 2017). In AML diagnosed in children under the age of 24 months, a chromosomal translocation t(7;12)(q36;p13) with poor prognosis has been reported, but not in acute lymphoid leukemia (ALL) (von Bergh et al., 2006). Studies have shown contradictory results on the incidence of t(7;12), with earlier studies suggesting the incidence of t(7;12) as high as 30% (von Bergh et al., 2006), but more recent studies suggesting the incidence to be 5-7% (Bolouri et al., 2018; Espersen et al., 2018). Similarly, different results have been reported regarding the prognosis of t(7;12), with earlier studies showing 3-year event free survival of 0% (von Bergh et al., 2006), but more recent studies showing 20%-43% 3-year event free survival (Bolouri et al., 2018) (Espersen et al., 2018), but with a very high relapse rate in all studies, ranging from 57-80% (Bolouri et al., 2018; Espersen et al., 2018). However, the understanding of the mechanisms behind the t(7;12) that causes leukemia transformation remains limited.

The chromosomal break-points have consistently been found to be located close to the Motor neuron and pancreas homeobox 1 (*MNX1)* gene in chromosome 7, and after exon 1 or 2 in the *ETV6* gene in chromosome 12 (Beverloo et al., 2001). The translocation leads to *MNX1* gene activation and, in about 50% of cases, to a *MNX1*::*ETV6* fusion transcript consisting of exon1 of *MNX1* transcript variant 1 spliced to the remaining ETV6 exons, depending on the location of the break point in ETV6 (Tosi et al., 2015).

MNX1 also known as Homeobox HB9 (*HLXB9*), belongs to the homeobox domain family of transcription factors, with previous studies showing the importance of *MNX1* in motor neuron development (Thaler et al., 1999), pancreas development (Harrison et al., 1999; Li et al., 1999)

and in hereditary sacral agenesis (Ross et al., 1998). *ETV6* also known as *TEL* belongs to the ETS-family transcription factors. *ETV6* encodes a transcriptional repressor that plays a critical role in hematopoiesis and in embryonic development, with more than 30 identified chromosomal translocations (Hock and Shimamura, 2017). *ETV6* expression is essential for normal HSC function as well as generation of thrombocytes by megakaryocytes, but not for other hematopoietic cells (Hock et al., 2004).

Translocations involving the chromosomal region of 12p13 that result in the rearrangements of the *ETV6* gene are one of the most commonly observed chromosomal abnormalities in human leukemia (De Braekeleer et al., 2012). ETV6 mediated leukaemogenesis can result from the ectopic expression of a proto-oncogene in the vicinity of a chromosomal translocation (Rawat et al., 2004) or the constitutive activation of the partner protein (Golub et al., 1994). In addition, formation of fusion protein can result in the modification of the original functions of a transcription factor (Zelent et al., 2004), or loss of function of the fusion gene, affecting *ETV6* and the partner gene (De Braekeleer et al., 2012).

The role of the MNX1::ETV6 fusion protein in the development of AML has not been established. It is also unclear whether the driver of leukemogenesis is the MNX1::ETV6 fusion or the simultaneous overexpression of MNX1. The aim of this study was to assess the transformation capacity and the molecular mechanism of the MNX1::ETV6 fusion and the ectopic expression of MNX1 *in vitro* and *in vivo* using murine transplantation models.

RESULTS

MNX1 *induces acute myeloid leukemia using hematopoietic cells of fetal origin*

To investigate the leukemogenic potential of the translocation t(7;12)(q36;p13), we transduced primary murine (C57BL/6) hematopoietic stem and progenitor cells (HSPC) from either adult bone marrow (ABM) after 5-FU stimulation or fetal liver (FL) cells at E14.5 with retroviral vectors for expression of the *MNX1::ETV6* fusion, *MNX1*, *ETV6* or empty vector (Ctrl). Expression of *MNX1*, *ETV6* and *MNX1::ETV6* fusion was first confirmed in both FL and ABM using qPCR (Supplement figure 1a and 1b) and western blotting (Supplement figure 1c). The transduced cells were transplanted into lethally irradiated immunocompetent C57BL/6 mice with rescue bone marrow. Neither *MNX1* overexpression nor the *MNX1::ETV6* fusion using either ABM or FL cells were able to induce leukemia in mice (Supplement figure 2a-d). Six months after transplantation, all mice were euthanized; blood and tissue samples were collected for hematological and histological evaluation. Mice transplanted with either ABM or FL showed no signs of leukemia, as determined by WBCs count, anemia, peripheral blood examination or spleen size (Supplement figure 2b and 2d). MNX1 chimerism in the (C57BL/6), as determined by percentage of GFP/YFP in the peripheral blood was very low compared to the other experimental arms, which displayed an initial high percentage with a gradual decline over the transplantation period (Supplement figure 3a). Increasing percentage of MNX1 chimerism through sublethal radiation with no rescue BM, as suggested by Andrade et al, 2011 (*20*) (Supplement figure 3b), resulted in 20% of the mice exhibiting signs of malignant transformation, including high WBCs count, severe anemia and enlarged spleen (Supplement figure 2e and 2f).

Since the chromosomal translocation t(7;12)(q36;p13) is only seen in children diagnosed with AML before the age of 24 months, with the majority diagnosed before six months of age, where

the immune system is also less developed (Espersen et al., 2018). We examined the leukemogenic potential of *MNX1* overexpression and the *MNX1::ETV6* fusion in immune-compromised mice. *MNX1::ETV6* fusion, *MNX1* overexpression, *ETV6* overexpression or empty vector (Ctrl) were retrovirally transduced into primary murine (C57BL/6) hematopoietic progenitor cells from fetal liver (FL) at E14.5. The cells were then transplanted into NOD.Cg-*Kit*$^{W-41J}$ *Tyr* $^{+}$ *Prkdc*^{scid} *Il2rg*^{tm1Wjl}/ThomJ (NBSGW) mice with no radiation. As shown in Figure 1, approximately 12 to18 weeks after transplant, the recipient *MNX1* mice showed clear signs indicative of leukemia development including pallor, weight loss and hunched postures. All mice exhibited leukocytosis with a high percentage of cells expressing MNX1 as indicated by GFP/YFP percentage, with elevated blast cells in both blood and bone marrow, severe anemia, enlarged spleens and liver, with infiltration of leukemic cells (Figure 1). Cells from bone marrow showed predominantly expression of the myeloid marker c-Kit but not the stem cell marker SCA-1 and was also negative for more differentiated myeloid markers such as MAC-1, LY6G1 and LY6C1, suggesting a poorly differentiated myeloid leukemia (Figure 1d). Similar results were seen in the C57BL/6 mice developing leukemia in the MNX1 sublethal radiation group, with cells from the bone marrow showing predominant expression of c-Kit (Supplement figure 3c).

As the immunocompromised NBSGW mice are characterized by enhanced enrichment of transplanted cells, in addition to the immunocompromised system. We set out to investigate the possibility that the leukemogenic effect of MNX1 in the immunocompromised mice might be, in fact, due to enhanced transplantation efficiency in the NBSGW mice. To address such hypothesis, we reduced the chimerism of transplanted MNX1 in the (NBSGW) mice through usage of lethal radiation and rescue bone marrow similar to the previous experiment in the (C57BL/6) mice, in comparison to sublethal radiation with no rescue BM. As shown in (Supplement figure 3d), although higher MNX1 chimerism resulted in a more rapid leukemia

induction, mice with lethal radiation and rescue bone marrow still exhibited leukemia but with a slightly longer latency. Further confirmation for acute leukemia induction by MNX1 was achieved after secondary transplant of BM from mice with primary leukemia, either with no radiation (Supplement figure 3e), or with sublethal radiation and rescue BM (Supplement figure 3f). Taken together, these results suggest that although the percentage of engraftment and chimerism of cells in BM might be a contributing factor, the main limiting factor for MNX1 leukemia induction appear to be the immune status of the mice. Finally, when immunocompromised (NBSGW) mice were transplanted with cells from ABM transduced with MNX1, there was no signs of leukemia (Supplement figure 4) six months after the transplant, suggesting that the leukemogenic potential of MNX1 requires hematopoietic cells from fetal origin.

MNX1 alters differentiation in favor of myeloid lineage while increasing proliferation and colony replating capacity of the cells

Primary murine (C57BL/6) HSPC from FL at E14.5 cells were transduced with *MNX1::ETV6* fusion, *MNX1*, *ETV6* or empty (Ctrl) retroviral vector and the immunophenotype of the cells was examined using flow cytometry. We found that both MNX1 and MNX1::ETV6 fusion altered differentiation in favor of myeloid lineage, with MNX1 showing more prominent effect with both myeloid markers; Mac-1 and Ly6C accompanied with the depletion of Lin-/Sca1+/c-kit+ (LSK) population, while MNX1::ETV6 fusion only showed upregulation of Ly6C (Figure 2a-c). MNX1 did not result in increasing CMP or GMP progenitor populations, but rather reduced the percentage of MEP population (Supplement figure 5a). Similar results were also shown with MNX1 expression in ABM but to a lower extent, while the MNX1::ETV6 fusion showed no effect in ABM (Supplement figure 5 b-d). Additionally, ectopic MNX1 lead to higher percentage of GEMM colonies and a reduction in BFU colonies (Figure 2d). Moreover,

only ectopic *MNX1* increased CFU replating capacity (Figure 2e) and the proliferation capacity of the FL cells (Figure 2f; Supplement figure 5f).

MNX1 induces DNA damage

To investigate the molecular pathway through which *MNX1* is mediating its leukemogenic effect, differential gene expression between *MNX1* leukemic BM cells, and FL with empty vector (Ctrl) were assessed using next generation RNA-sequencing (Figure 3a-d, Supplement figure 6b). The expression of *MNX1* from the leukemia BM cells was confirmed in all samples using qPCR prior to RNA-sequencing (Supplement figure 6a). Applying gene set enrichment analysis (GSEA) with Nominal p value ≤ 0.05 (Figure 3d) , and gene ontology biological (GO) pathway enrichment analysis with FDR ≤ 0.05 (Supplement figure 6b) , we found that the highest enriched pathways for *MNX1* overexpression involved DNA damage, cell cycle, chromatin organization, methylation of histones, metabolic processes, megakaryocyte, and myeloid cell differentiation pathways (Figure 3d; Supplement figure 6b). Similar results were seen using a different control with BM taken from mice transplanted with FL cells with empty vector (Ctrl) (Supplement figure 6c-e).

Enrichment of genes involved in DNA double strand break repair (Supplement figure 6f) could explain the reduction of hematopoietic stem cells, altered differentiation towards myeloid lineage and increase of the oncogenic potential of cells as described by Mandal and Rossi, 2012 (Mandal and Rossi, 2012). We thus, examined γH2AX foci induction in FL and ABM cells one week after transduction. *MNX1* and to a lower extend *MNX1::ETV6* fusion induced higher number of γH2AX, indicative of higher DNA damage in both ABM and FL (Figure 4a; Supplement figure 7a). Next, we investigated the consequence of such induced DNA damage, and found that it was accompanied with G1 cell cycle accumulation and less cells in S-phase of the cell cycle for both *MNX1* and *MNX1::ETV6* fusion transduced FL cells. However, no

effect was observed in ABM cells (Figure 4b). Following up on the cell cycle distribution, we observed that the reduction in S-phase was only a transient event, which was resolved one week after in the FL cells (Supplement figure 7b). Surprisingly with the ABM cells, most of the cells disappeared and were replaced by a Sub-G1 peak suggestive of apoptotic cells (Supplement figure 7b). To confirm this observation, Annexin-V and DAPI were used to detect apoptotic cells, as shown in Figure 4c. ABM cells showed an apoptotic induction in MNX1 cells reaching 3.5-4-fold increase. Such pronounced apoptotic induction was not seen in FL cells (Figure 4c). This could provide a possible explanation for the leukemic transformation only seen in mice transplanted with FL cells and not with ABM cells.

To follow up the consequences of *MNX1* induced DNA damage in the leukemic mice, BM from *MNX1* induced leukemia mice were analyzed for cell cycle distribution in comparison with BM from Ctrl mice. As shown in Figure 4d and Supplement figure 7c, the median value of the DNA from the leukemia BM was higher than that from the Ctrl mice, suggesting an increase in the amount of DNA or a hyperploidy in the leukemia BM.

An interesting candidate for the observed DNA damage, which was found enriched in several pathways that may contribute to DNA damage including, Kinetochore and microtubule anchoring was the centrosomal protein 164 (*Cep164*). *Cep164* encodes a protein which is involved in microtubule organization, chromosome segregation during mitotic phase of cell cycle and DNA repair (Pan and Lee, 2009; Sivasubramaniam et al., 2008),

Results from RNA-Seq was confirmed using qPCR for both FL cells and leukemia BM (Figure 5a), and further confirmation for the direct role of MNX1 on *Cep164* expression was achieved through determining the binding of MNX1 to the promoter of *Cep164* using ChIP-qPCR (figure 5b). Using the mouse genome browser, we found that the same promoter region through which MNX1 binds to at the *Cep164* gene, exhibited histone modifications namely H3K4me3 and

H3K27me3. This was confirmed using ChIP-qPCR for both H3K4me3 and H3K27me3 on the same promoter region (Supplement figure 7d).

MNX1 mediates leukemogenesis through altered histone modifications.

Western blotting for both H3K4me3 and H3K27me3 revealed that the histone modifications was in fact a global effect induced by MNX1 (Figure 5c, supplement figure 7e), and co-immunoprecipitation experiments (Co-IP) showed the association of MNX1 to histone H3 (Supplement figure 7f), suggesting that MNX1 might mediate its effects through protein-protein interaction, which induces changes in histone modifications. Western blot analysis revealed an increase in both the mono and di-methylation of the H3K4 as well (Figure 5c, supplement figure 7e). Antibody-guided chromatin tagmentation sequencing (ACT-Seq) was used for mapping genome-wide distribution of the histone modifications (Figure 5d). We found that H3K27me3 histone modification showed a decreased number of differentially accessible regions in comparison with Ctrl FL cells (FDR ≤ 0.05, log2 fold change $\geq |1|$), involving mainly distal intergenic regions followed by promoter and other intronic regions (Figure 5d). To follow up the consequences of these histone modifications, we preformed ATAC-Seq to detect chromatin accessibility. Our data showed that MNX1 BM cells exhibited increased number of differentially accessible chromatin regions in comparison with Ctrl FL cells (FDR ≤ 0.05, log2 fold change $\geq |1|$) (Figure 5e), involving promoters mainly, followed by distal intergenic and intronic regions, very similar to pattern showed by H3K27me3 (Figure 5d-e).

Pathway analysis of genes annotated to differentially accessible regions from ATAC-Seq (FDR ≤ 0.05, log2 fold change $\geq |1|$) revealed similar pathway enrichment to the RNA-Seq, with high enrichment in metabolic pathways, myeloid cell differentiation, erythrocyte differentiation, cytoskeleton organization, cell cycle process and apoptotic cell process (Supplement figure 7g). Further analysis through integrating ATAC-Seq data with in-silico predicted transcription

factor (TF) binding sites by DiffTF package, revealed 130 differentially activated TFs (FDR < 0.05) between MNX1 BM from leukemia mice and FL Ctrl cells (Table 1, Supplement figure 8a). Analysis of the identified TFs revealed enrichment for myeloid/erythrocyte differentiation, cellular metabolism, G1/S-phase transition of cell cycle, histone methylation, DNA methylation and DNA damage response transcription factors; including regions with increased accessibility for *Tal1a*, *Gata2*, *Gata1*, *Foxo3*, *Klf1*, *Snai2* and *Klf4* and regions with decreased accessibility for *Jun*, *Fosl1*, *Batf*, *Stat*, *Gfl1*, *Cebpa* (Table1, Supplement figure 8a). Finally, correlation analysis between differentially accessible chromatin regions from ATAC-Seq and differentially expressed genes from RNA-Seq, revealed a highly significant association with r=0.47 (Pearson correlation) (Supplement figure 8b). Overall, these results suggested a possible epigenetic role for MNX1 in inducing a global histone modification that is affecting chromatin accessibility and inducing differential gene regulation.

To address this hypothesis, proteins associated with MNX1 were studied using co-immunoprecipitation with anti-HA antibodies to pull down MNX1 followed by a mass spectrometric analysis. This was done in two independent experiments and compared to FL cells transduced with empty vector as negative control (Supplement table 1). Proteins that were common between the two experiments and that were absent in the negative control (total of 232 proteins, highlighted in Supplement table 1), were used for further analysis. Pathway analysis using STRING for protein-protein interactions in reactome pathways for the identified proteins revealed a high enrichment for methylation pathway (Figure 5f, Table 2), namely MAT2A, MAT2B and AHCY, in addition to several SAM-dependent methyl transferase and downstream targets including Tfb1m, Trmt112, Mthfd2, Shmt2, Wdr5, Eed and the histone demethylase Jmjd6 (Supplement table 1). The association of MNX1 to both MAT2A and AHCY was confirmed using Co-IP (Figure 5g, supplement figure 8c), and total protein

expression level using western blotting revealed no change for both MAT2A and AHCY expression levels (Supplement figure 8d).

The methylation pathway is utilized by the cell to convert the methionine amino acid to the universal methyl donor S-adenosyl-methionine (SAM), which upon donation of its methyl group is converted to S-adenosyl-homocysteine (SAH). SAM is then used as a cofactor in most methylation reactions by SAM-dependent methyltransferases, catalyzed by methionine adenosyl transferases (MAT) (Kaiser, 2020; Sanderson et al., 2019). To investigate the role of MNX1 in altering the methylation pathway and methionine cycle, free methionine concentrations, along with various amino acids concentrations were determined in both FL cells and in leukemia BM cells using LC-ESI-MSMS (Figure 5h; Supplement figure 8e). SAH concentration was determined using ELISA and was normalized against the protein concentration as determined by BCA (Supplement figure 8f, see materials and methods for details). As shown in Figure 5h and supplement figure 8f, MNX1 overexpression increased the concentration of SAH and induced reduction in the free methionine. To confirm the role of MNX1 protein complex in histone methyltransferase, MNX1 was pulled down with Co-IP and incubated with recombinant Histone H3. Methylation of Histone H3 was detected both using anti-methylated lysine antibody and H3K4me1 antibody (Figure 5i, Supplement figure 8g).

Finally to confirm our observation on the role of MNX1 in interaction with methionine cycle and association with methyltransferases as the driving factor for MNX1 phenotype, we used Sinefungin, a natural nucleoside analogue of S-adenosylmethionine, that act as a SAM competitor and accordingly a pan methyltranferases inhibitor (Zhang and Zheng, 2016). Adding 5µM of Sinefungin to FL cells with ectopic expression of MNX1, partially or completely prevented the effects of MNX1 on histone modifications (Figure 6a, Supplement figure 9a), DNA damage induction (Figure 6b; Supplement figure 9b), cell cycle distribution

(Supplement figure 9c), myeloid differentiation and LSK depletion (Figure 6c-d). Furthermore, MNX1 FL cells treated *in vitro* with Sinefungin and then transplanted into NBSGW mice did not show any signs of leukemia transformation (Figure 6e; Supplement figure 9d-e), without affecting the MNX1 expression (Supplement figure 9f). The presence of viable cells after treatment in the transplantable mice was confirmed through the detection of GFP/YFP chimerism in peripheral blood every 2 weeks (Supplement figure 9g).

To confirm that Sinefungin treatment prevented leukemia transformation through inhibition of methyltransferase activity in complex with MNX1 and not the methyltransferase activity downstream of MNX1 ectopic expression, RNA sequencing was done before and after treatment with Sinefungin. Differentially expressed genes (FDR ≤ 0.05, log2 fold change $\geq |1.5|$) from MNX1 cells after treatment (MNX+S) were clustered with MNX1 (Figure 6f), and many of the differentially expressed genes by MNX1 overexpression remained at similar level after treatment (Supplement figure 9h), suggesting a limited effect of Sinefungin on downstream targets of MNX1 ectopic expression. Further confirmation was achieved by studying the RNA expression of FL cells transduced with MNX1 or empty vector before transplantation in mice. As shown in supplement figure 10, genes involved in H3K4 methylation pathways were only overexpressed in MNX1 cells from BM of leukemic mice and not in the pre-transplantation FL cells with MNX1. *Mat2a* (Log fold change (LogFC 1), FDR ≤ 0.05) and *Mat2b* (LogFC 1.3, FDR ≤ 0.05) were only overexpressed in BM from leukemia mice with MNX1 (Table 3). Taken together, these data suggest that association of MNX1 with methionine cycle/methyl transferases in a protein complex occurs upstream and prior to their overexpression.

Human IPSC with t(7;12) showing similar pathway enrichment as the mouse model

Finally in order to confirm the events occurring in our mouse model were relevant to human t(7;12) patients, we have created human induced pluripotent stem cell (iPSC) line that carry the translocation t(7;12) using CRISPR/Cas9 (Nilsson et al., 2022). The t(7;12) iPSC, when induced to differentiate into HSPC (iHSPC), showed a dramatic increased expression of *MNX1* compared with the parental iPSC and exhibited, similarly to the mouse FL cells, blockage in erythroid and megakaryocytic lineages and altered myeloid differentiation (Nilsson et al., 2022). Comparing the transcriptome enriched pathway analysis of the t(7;12) iHSPC with leukemia cells from our mouse model revealed high degree of common pathway activation (Figure 6g), with 72% of pathways in human iHSPC common with our mouse model (Figure 6g). The common pathways included metabolic processes, myeloid cell differentiation, DNA-repair, methylation, chromosome organization and histone modifications (Figure 6g). Furthermore, CEP164 (LogFC 1.4, FDR $\leq$ 0.05), MAT2A (LogFC 0.23, FDR $\leq$ 0.05) and AHCY (LogFC 0.4, FDR $\leq$ 0.05) upregulation was also shown in the iPSC t(7;12) model (Table 3, (Nilsson et al., 2022)).

Using children's oncology group (COG)–National Cancer Institute (NCI) TARGET AML initiative data set, RPKM counts from RNA-Seq of pediatric AML patients (available at https://target-data.nci.nih.gov/Public/AML/mRNA-seq/), was studied for the expression of *MNX1* in t(7;12) patients, and the associated expression of *CEP164* and *MAT2A* in these patients (Supplement figure 11). The cutoff was RPKM = 0.3 for *MNX1*. Data from eight patient samples was obtained with RPKM $\geq$ 0.3, which showed an elevated expression of *MNX1* only in t(7;12) patients. Similarly, *MAT2A* and *CEP164* showed elevated RPKM values in these t(7;12) the patient samples, (Supplement figure 11 a).

In conclusion, our data provide biological and clinical significance for MNX1 expression in pediatric AML and suggesting a mechanism through which MNX1 is mediating the leukemogenic effect through the aberrant methylation that result in histone modifications, DNA damage and leukemia transformation (Figure 6h).

DISCUSSION

The t(7;12) rearrangement is a cytogenetic aberration that has been reported in children diagnosed with AML under the age of 24 months. The function of this translocation in inducing children's leukemia and the reason for its absence in adult leukemia was unknown, and whether the translocation served as a driver for children's leukemia or present after leukemia induction was poorly understood (Tosi et al., 2015). In the current study using a murine model we showed that the ectopic expression of MNX1 rather than the MNX1::ETV6 fusion protein was able to initiate and drive leukemogenesis. This has been further confirmed by a recent study from our group, where a dramatic increase in expression of MNX1 was seen using human iPSC line engine with CRISPR/Cas9, to carry the translocation t(7;12). The malignant transformation in our mouse model mediated by MNX1 overexpression matched the criteria for AML (Kogan et al., 2002), where the development of leukemia was rapidly fatal in both primary transplanted mice as well as in secondary recipient. The percentage of blasts in peripheral blood was more than 20%, mainly involving the hematopoietic tissues of bone marrow and spleen and was accompanied by anemia and leukocytosis. The majority of the cells were highly positive for CD117 (c-Kit) but lacked other typical myeloid markers, with percentage of bone marrow engraftment ranging between 60-90%, compatible with an AML without maturation. Our data showed that ectopic expression of MNX1 was only able to induce AML using HSPC from fetal origin and not from adult bone marrow, primarily in immunocompromised mice. This is interesting in the light of the clinical observation that this AML subtype is only found in very young children with peak at six months where the immune system is still under development (Espersen et al., 2018; Tosi et al., 2015). One possible explanation for the incapability of MNX1 ectopic expression to induce leukemia from adult progenitor hematopoietic cells was further suggested in our study, as the ectopic expression of *MNX1* in these cells resulted in dramatic apoptotic induction, which was not observed in hematopoietic progenitor cells from

fetal origin. This could be due to the difference in gene expression, metabolic demand, cell cycle profiles between adult and fetal stem cells (Bowie et al., 2007; Chen et al., 2019; Manesia et al., 2015), the different hematopoietic lineage and progenitor population between fetal and adult stem cells (Copley and Eaves, 2013), or due to the presence of naturally occurring DNA damage in the adult stem cells (Biechonski et al., 2017), thus making the cells more susceptible for apoptotic induction with additional DNA damage induced by MNX1.

It's also important to note that when using radiation in the immunocompromised (NBSGW) mice, 10-20% of the control mice developed leukemia. However, these control leukemia mice were exhibiting different differentiation markers as they were negative for (c-KIT) and were unable to induce acute leukemia in NBSGW mice after secondary transplant unlike the MNX1 induced leukemia (Supplement figure 3f). Leukemia induction in these control mice, might be a consequence of the sensitivity of these mice for radiation (McIntosh and Brown, 2015). Thus, we used NBSGW mice with no radiation as our main mouse model.

Studying the mechanism of MNX1 *in vitro* revealed an induction in DNA damage both in FL cells and ABM cells, which could contribute to the observed skewed differentiation towards myeloid lineage evident by the depletion of LSK and MEP population and increased Mac1 and Ly6C population. The notion that DNA damage in stem cells might influence differentiation was first demonstrated in melanocyte stem cells (MSCs), where irreparable DNA damage, caused by ionizing radiation triggered MSC differentiation into mature melanocytes (Inomata et al., 2009). With respect to hematopoietic stem cells, DNA damage was found to induce differentiation towards lymphoid lineage (Mandal and Rossi, 2012), or myeloid lineage (Beerman et al., 2010) with regards to the composition of the HSC pool harboring an increase, decrease of a balanced percentage of myeloid-biased vs. lymphoid-biased HSCs (Beerman et al., 2010; Cho et al., 2008). This lead to the assumption that DNA damage might be responsible

for the skewed differentiation in the aging hematopoietic system towards myelopoiesis which is characterized by an increasing percentage of myeloid-biased HSCs (Beerman et al., 2010; Cho et al., 2008; Mandal and Rossi, 2012; Scheffold et al., 2020). The consequence of this DNA damage was evident in the BM from the leukemia mice with increased DNA content associated with hyperploidy. This shows a resemblance to the clinical presentation where t(7;12) is associated with complex karyotype in the majority of cases (Bolouri et al., 2018; Espersen et al., 2018). The observed DNA damage would further illustrate the interplay between MNX1 increased leukemogenicity as evident by leukemia induction, increased proliferation, and colony replating capacity and the LSK depletion/ skewed myeloid differentiation.

Molecularly we found MNX1 to associate with members of the methionine cycle, including MAT2A, AHCY and MAT2B, in addition to several downstream SAM-dependent methyl transferases including Tfb1m, Trmt112, Mthfd2, Shmt2, Wdr5, Eed and the histone demethylase Jmjd6. Methionine is an essential amino acid. It is converted to the universal methyl donor S-adenosyl-methionine (SAM), which upon donation of its methyl group is converted to S-adenosyl-homocysteine (SAH). This reaction is catalyzed by methionine adenosyl transferases (MAT). SAM is used as a cofactor in most methylation reactions and provides the activated methyl group for methylation of proteins, including histones, DNA, RNA and lipids. These methylation events are highly dependent on methionine metabolism, with alterations in methionine showing profound effects on DNA and histone methylation (reviewed in (Kaiser, 2020; Sanderson et al., 2019)). SAM also interacts with demethylase enzymes to inhibit their demethylase activity (Detich et al., 2003), and loss of methylation promotes demethylation of histones through demethylase enzymes (Ye et al., 2019). Here, the consequences of MNX1 effect on methylation and methionine cycle was observed through altered histone methylation, namely H3K4me mono, di and trimethylation and H3K27me3,

which resulted in altered chromatin accessibility as seen by ATAC-Seq analysis. The role of MNX1 in methylation/methyl-transferase was shown by; decline in the free methionine concentration; elevated SAH concentration; the association of MNX1 to MAT2A and AHCY in addition to several downstream SAM-dependent methyl transferase; the global alteration of histone methylation H3K4me and H2K27me3; methylation of recombinant Histone H3 by MNX1 complex *invitro;* pathway analysis of RNA-seq and ATAC-Seq from mouse model and RNA-seq from the human iPSC model which showed enrichment in the methylation pathway, in addition to protein metabolism, a downstream pathway of methionine cycle (Parkhitko et al., 2019; Sanderson et al., 2019) and nucleic acid/lipid metabolism a downstream pathway of the methionine-closely linked folate cycle (Zarou et al., 2021; Zheng and Cantley, 2019),. This is in addition to the complete or partial prevention of MNX1 phenotype through usage of the SAM/SAH analog Sinefungin (Couture et al., 2006; Fuller and Nagarajan, 1978).

The role of homeodomain proteins in recruiting methyltransferase to regulate gene expression and chromatin structure through histone modifications, has been shown previously as a mechanism of regulating the differentiation of myoblasts by MSX1 (Wang and Abate-Shen, 2012; Wang et al., 2011). This would suggest the binding and association of MNX1 with methyltranferases and members of methionine cycle, and the subsequent change in chromatin structure and histone modifications could be the physiological role for MNX1 during differentiation (Dalgin et al., 2011; Leotta et al., 2014), and the abnormal expression of MNX1 in hematopoietic cells might act as the driver of leukemia transformation. This is further supported by recent findings which showed MNX1 binding to loci on chromatin to be enriched for H3K4me1 and H3K4me3 during neural development (Sun et al., 2021).

.

In conclusion, our results provide biological and clinical significance for MNX1 expression in pediatric AML, and give the rationale for targeting methylation, methionine cycle or other MNX1 downstream pathways as a treatment strategy for AML patients with t(7;12).

MATERIAL AND METHODS

Plasmid constructions

The *MNX1*, *ETV6* and MNX1::ETV6 fusion sequences are listed in Supplement table. 2. An HA-tag (36bp) is introduced at the 5' end and via a linker sequence of 24 bp attached to the separate gene sequences where the first ATG is removed. These constructs were cloned into the MSCV-IRES-GFP and MSCV-IRES-YFP vectors (Takara, Japan) #634401 under control of the viral LTR promoter.

Generation of transduced murine bone marrow (BM) cells and transplantation assays

Mice were bred and maintained at the Gothenburg university laboratory for experimental biomedicine Animal Facility (Gothenburg, Sweden) in an SPF environment. All experimental protocols were approved by the state government of Gothenburg, Sweden. Establishment and characterization of BM cell lines following transduction of BM cells with *MNX1*, *MNX1::ETV6*, *ETV6* or empty vector Ctrl have been done as described previously (Arabanian et al., 2018). In brief, BM cell lines were established from BM cells previously treated with 5-fluorouracil (5-FU) from 8-12 weeks old (C57Bl/6) mice (Charles River Laboratories, Inc., Wilmington, Massachusetts, USA) for three days for adult bone marrow (ABM) or from fetal liver at embryonic days 14.5 (E14.5) and maintained in liquid culture (Dulbecco's modified Eagle's medium supplemented with 18% fetal bovine serum, 10 ng/mL human interleukin [IL]-6, 6 ng/mL murine IL-3, and 50 ng/mL murine stem cell factor). All culture media were obtained from Sigma and recombinant growth factors from Peprotech. To generate *MNX1*, *MNX1::ETV6* , *ETV6* or empty vector Ctrl BM cell lines, the BM cells were transduced by cocultivation on irradiated (4000 cGy) E86 producers (ATCC, Manassas, VA, USA) for a period of 2 days in the presence of 5 μg/mL protamine sulfate (Sigma). Cells were sorted for GFP^+ and/or YFP^+ expression by flow cytometry analysis (fluorescence-activated cell sorting

[FACS]) FACSAria (BD Biosciences) and maintained in culture for 5-7 days post transduction before transplantation in mice. Lethally (8.5 Gy) or sublethally (5.5 Gy) radiated 8-12 weeks old C57Bl/6 mice received the equivalent of 0.6×10^6 rescue BM cells and/or $0.8\text{-}1\times10^6$ transduced cells via tail vein injection. For immunocompromised NOD.Cg-*Kit*$^{W\text{-}41J}$ *Tyr* $^{+}$ *Prkdc*^{scid} *Il2rg*^{tm1Wjl}/ThomJ (NBSGW) mice (The Jackson Laboratory, Bar Harbor, ME, USA), cells were transplanted either with no radiation, or after lethal dose of (1.6 Gy) and sublethal dose of (0.9 Gy). Donor-derived engraftment and reconstitution were monitored by flow cytometry analysis for GFP^+ and/or YFP^+ expression in the peripheral blood of the transplants every 2 weeks. Mice were sacrificed using Isoflurane (Baxter, Deerfield, IL, USA). Blood counts were analyzed on a Sysmex KX-21 Hematology Analyzer (Sysmex, Norderstedt, Germany).

Immunophenotyping and flowcytometry

Cells were collected 1-2 weeks after transduction. Then they were washed twice with PBS, blocked with 0.1% FBS, mouse BD FC Block #553142 (BD Biosciences) in PBS for 10 mins RT. Then incubated with the antibodies for 20 minutes at RT, washed and resuspended in PBS. The following antibodies were purchased from BD Biosciences. Sca1-V450#560653, Cd3e-V450#560801, Ter119-V450#560504, CD45R-V450#560473, Ly6G/Ly6C-V450#560454, Mac1-V450#560455, Ly6G-PeCy7#560601, B220-V450#560472, CD127-V450#561205, cKit-APC#553356, Sca1-PeCy7#558162, CD45-APCCy7#561037, Ter119-APC#561033, CD8a-APCCy7#561967, CD4-APCCy7#561830. The following from (Thermo Fisher Scientific). CD115-APC#17-1152-80, CD64-APCCy7#47-0641-82.

For cell cycle analysis, the proportion of cells in G_1 and G_2 phases were measured by staining with DAPI (BD Biosciences, #564901) as described previously (Waraky et al., 2014). Briefly, cells were washed with PBS, and stained DAPI solution 1:100 containing RNase A (250

μg/ml) and 0.25% Triton X100 for 15 min at room temperature. The samples were processed using FACSAria (BD Biosciences), and the data were analyzed with the Cell Quest software (BD Biosciences) or with flowing software v 2.5.1 (Turku bioscience center, Finland).

Apoptosis analysis was studied using Annexin V/DAPI method (Annexin V-FLUOS staining kit, Roche, Mannheim, Germany) according to the manufacturer's protocol using AnexinV-APC antibody#550474 (BD Biosciences) and DAPI. Flow cytometric analysis was immediately performed using FACSAria.

Western blotting

Cells were lysed in modified RIPA buffer (50 mm Tris, pH 7.4, 150 mm NaCl, 1% Nonidet P-40, 1 mm EDTA, 0.25% sodium deoxycholate) containing protease (Roche Applied Science, Mannheim, Germany) and phosphatase (Sigma) inhibitors and processed as described previously (Waraky et al., 2017). Cell lysate subjected to sonication using bioruptor for 5 minutes (30 second ON/ 30 seconds OFF). Primary antibodies used in this study included the following: rabbit-anti HA # 11846, rabbit-anti actin # 4970, rabbit-anti H3K4me1 #5326, rabbit-anti H3K4me2 #9725 from Cell Signaling Technology, rabbit-anti Mat2A#NB110-94158, rabbit-anti Ahcy #NBP2-48817 from Novous biological, rabbit-anti H3K4me3 (catalog no. C15410003-50), rabbit anti-H3K27me3 (catalog no. C15410069), from Diagenode and rabbit anti-Histone 3 (catalog no. Ab18521) from Abcam.

Immunoprecipitation and mass spectrometry

Anti HA-magnetic beads from Thermo Fisher Scientific (catalog no. 88836) were used for immunoprecipitation. After blocking with 0.1% BSA in PBS, 0.7-1 mg of cell lysates were incubated with HA antibody for 1h at RT. For IgG antibody, the antibody was cross-linked to magnetic protein G Dynabeads using Dynabeads® antibody coupling kit 14311D (Invitrogen).

The immune complexes were washed three times with lysis buffer and eluted by boiling in SDS sample buffer (Invitrogen). Precipitates were separated with SDS-PAGE and co-precipitated protein bands were visualized using Coomassie Blue. Prominent gel bands were excised for LC-MS using a hybrid LTQ-Orbitrap Velos mass spectrometer (Thermo Fisher Scientific) as described in (Waraky et al., 2017).

Invitro histone methyltransferase

Invitro histone methyltransferase was done as described in (Jacob and Voigt, 2018). Briefly, 0.25-0.5 mg of cell lysates were incubated with HA antibody for 1h at RT. The immune complexes were washed three times with lysis buffer and once with BC100 buffer (20 mM Tris–HCl pH 8.0, 100 mM KCl, 0.2 mM EDTA, 20% glycerol, 1 mM DTT). The immune complexes was incubated with 4 µg of human recombinant histone H3.1 and H3.3 (New England biolabs # M2507S, # M2503S) at 30 °C for 60 min in 25 µl of methylation buffer buffer (50 mM Tris–HCl pH 8.5, 5 mM MgCl2) in the presence of 10 µM SAM (New England biolabs # B9003S) and 4mM DTT. Omission of the recombinant histone H3, or the immune complexes served as negative controls. The reactions were terminated by boiling in SDS sample buffer (Invitrogen), followed by separations in 12% SDS-PAGE and immunoblottings using H3k4m31 (Cell signaling), Histone H3 (Abcam) and anti-methlylated lysines (Abcam #ab23366). Quantification was done using ImageJ (Schneider et al., 2012).

Histological preparation

Moribund mice or mice at the end of the experiment were euthanized. Liver, spleen, and sternum were harvested by fixing in 4% formaldehyde at 4°C, dehydrated in 70–100% ethanol, cleared in xylene and embedded in paraffin. Sections (4–5 µm). Paraffin-embedded tissue

sections were prepared at Histocentre (Gothenburg, Sweden) and stained with HandE. Blood samples was collected directly from the heart after euthanizing the mice , prepared as thin blood films, Giemsa-stained and examined under the microscope (Nikon Inc., Japan).

Colony forming unit assay

Methocult M3434 (STEMCELL Technologies) was used for the CFU assays where 5000 cells were seeded/petri dish and incubated for 7-14 days according to the manufacturer's protocol.

Proliferation assay

Cell proliferation was determined using MTT (3-[4,5-dimethylthiazol-2-yl]-2,5-diphenyltetrazolium bromide) assay from abcam # ab211091. Briefly, FL cells transducted with our constructs were plated, in triplicate, in a 96-well culture plate at 37° C in CO2 incubator for 7 days. Each day an equal volume of MTT was added to the cell culture medium. The plate was incubated at 37° C for 4 h followed by addition of MTT solvent. The plate was then swirled gently until all crystals are dissolved. Absorbance values were blanked against cell culture medium without cells. The absorbance was read at 590 nm using a microplate reader (Infinite F50®Tecan Group Ltd., Swiss). The absorbance was plotted against the number of days

Sinefungin treatment

Sinefungin was purchased from Calbiochem #567051 as Insolution. Final doses of 5µM was used to treat the cells. Daily change of medium with fresh Sinefungin was added after viral transfection for one week.

Gene expression analysis

Total RNA was isolated using the miRNeasy Plus micro kit (Qiagen) and cDNA synthesized with SuperScript III First-Strand Synthesis SuperMix for qRT-PCR (Invitrogen/Thermo Fisher

Scientific). TaqMan Gene Expression Assays and TaqMan Universal MasterMix II (Applied Biosystems/ Thermo Fisher Scientific) were used for probe based qPCR assays, listed in supplement table 2. A SYBR Green assay was used for the MNX1, ETV6 and MNX1(ex1)::ETV6(ex3) fusion detection, with primers synthetized at IDT (Integrated DNA Technologies) and Power SYBR Green PCR Master Mix (Applied Biosystems/Thermo Fisher Scientific), listed in supplement table 2. The reactions were performed on the ABI 7900HT Sequence Detection System (Applied Biosystems/ Thermo Fisher Scientific) with *hprt* as the reference gene. Gene expression was calculated using the deltaCt method and are presented as $2^{-deltaCt}$.

Next-generation sequencing

Total RNA was extracted from transduced FL cells after one week of transfection using RepliePrep RNA miniprep systems (Promega). 5-20µg of total RNA were utilized for RNA-Seq using DNBseq technology at Beijing Genomics Institute (BGI, Hong Kong), with RIN value of ≥7.5 and 100bp paired-end reads. An average of 40 million reads were generated for each sample. The gene expression level was quantified by BGI Europe. Only samples with 28S/18S ≥1, Q20_rate ≥ 97 and GC% ≥ 51% were used. For RNA-seq analysis, alignment was carried out to reference mouse genome GRCm38 using STAR (version 2.9.0a) with the following parameters: outSAMtype BAM SortedByCoordinate. Quantification was carried out using HTSeq-count (Python package HTSeq, python v 3.8.1) software using the following parameters -f bam -r pos -s no -m union with the reference annotation file. The mouse reference genome and annotation files were obtained from the Ensembl database. Differential gene expression was performed using the R package “Deseq2” (Love et al., 2014). Genes with log2 (foldchange) 1 and false recovery rate (FDR) adjusted p-value < 0.05 were considered differentially expressed genes. Principal component (PCA) analysis, heatmap analysis

(pheatmap) and enhanced volcano plot (enhancedVolcano) were performed in order to examine the level of differences in the gene expression profiles between control and MNX1 samples. Gene Ontology Go-biological process database was used for pathway analysis using the default parameters. A pathway was considered to be significantly enriched for a FDR < 0.05, p-value < 0.05 of the respective pathway. Gene Set Enrichment Analysis (GSEA) was used with the Gene ontology GO-biological process gene set. A pathway in GSEA analysis was regarded significant at nominal p-value < 0.05.

Assay for transposase-accessible chromatin using sequencing (ATACseq)

ATACseq libraries were prepared according to a modified Omni-ATAC protocol (Corces et al., 2017) as follows. Cells stored at -80 °C in culture medium containing 10% DMSO were thawed on ice, counted with a Countess counter (Invitrogen), pelleted at 1000 × g for 10 min at 4 °C, and a suitable aliquot for both ATACseq and antibody-guided chromatin tagmentation (ACTseq) was resuspended in cold phosphate-buffered saline (PBS) at a titer of 10^6 viable cells/ml. An aliquot of 50000 viable cells was pelleted at 600 × g for 5 min at 4 °C, and cells were resuspended in 50 µl cold RSB containing each 0.1% of NP40 and Tween-20 and 0.01% digitonin. Proper lysis was monitored microscopically using Trypan blue, then 200 µl RSB containing 0.1% Tween-20 were mixed in. Lysed cells were spun with 1000 x g for 10 min at 4 °C and resuspended in 48 µl transposition buffer (10 mM Tris-acetate, pH 7.6, 5 mM $MgCl_2$, 10% dimethylformamide, 30% PBS, 0.01% digitonin and 0.1% Tween-20). The suspension was completed by addition of 2 µl Tn*5* transposome generated as described by Picelli et al. (Picelli et al., 2014). (The Tn*5* transposase was kindly provided by the EMBL-Heidelberg protein expression and purification core facility). Tagmentation was performed at 37 °C for 30 minutes in a thermomixer with 1000 rpm. DNA was purified after addition of 20 µl 5 M guanidinium-thiocyanate with 140 µl HighPrep beads (Biozym) and eluted with 20 µl H_2O.

Sequencing libraries were generated by addition of 25 µl NEBNext High Fidelity 2× Master Mix (NEB), each 2.5 µl of 10 µM primer Tn5mCP1n and Tn5mCBar (Weichenhan et al., 2018) and 0.5 µl of 100x SYBRGreen I using a LightCycler 480 real-time machine with 72 °C for 5 min, 98 °C for 30 sec and cycling at 98 °C, 10 sec; 63 °C, 30 sec; 72 °C, 30 sec. Amplification was stopped when an increase of about 10 fluorescence units was observed, usually between cycle 12 and 15. . Libraries were bead-purified with 70 µl HighPrep beads and eluted with 12 µl EB (Qiagen). Concentrations and fragment lengths were determined with the Qubit dsDNA High sensitivity kit (Invitrogen) and the TapeStation D1000 High sensitivity assay (Agilent), respectively. Up to ten libraries with compatible barcodes were pooled equimolarly, and pools of 5-10 nM were sequenced in the DKFZ Genomics and Proteomics Core Facility (GPCF) using an Illumina NextSeq 550 system with 75 bp paired-end, mid output mode. Sequencing reads were bioinformatically analyzed as detailed by Hey et al. (Hey et al., 2021). In short, peak calling of processed reads was done using MACS2 callpeak v. 2.1.0.20140616 with a q-value cutoff of 0.05 and default parameters. The analysis is a publicly accessible fully containerized workflow using Common Workflow Language v. 1.0 (https://doi.org/10.6084/m9.figshare.3115156.v2); Highly Portable Processing of Data Generated by ChIP-seq, ChIPmentation, Cut&Run, and ACT-seq. Verion 1.1.2, Zenodo: Temple, FL, USA). Differentially accessible regions (DARs) were identified with the DiffBind R package (R package version 2.12.0) (Ross-Innes et al., 2012). Common peaks were considered those found in at least two samples. Differential analysis was performed using edgeR (Robinson et al., 2010). Regions with an FDR < 0.05 were considered differentially accessible. Further annotation of DARs was performed with R package ChIPseeker (R package version 1.20.0) (Yu et al., 2015). Differential transcription factor activity was predicted using diffTF (Berest et al., 2019) and in silico predicted transcription factor binding sites based on the HOCOMOCO 10 database were used as a reference (Kulakovskiy et al., 2018).

Antibody-guided chromatin tagmentation followed by sequencing (ACTseq)

ACTseq (Carter et al., 2019) was essentially performed as detailed by Liu et al. (Liu et al., 2021). As described in the ATACseq methods chapter, frozen cells were thawed, washed with PBS and, per antibody, aliquots of 50000 viable cells were lysed. Antibodies used for the pA-Tn*5* transposome-antibody complexes were directed against H3K27me3 (Cell signaling, 9733), IgG (Millipore PP64B) and yeast histone H2B (M3930, Boster Bio. Tech., Pleasanton, CA, USA), the latter complexes being used for spike-in to enable sequence read normalization between biological replicates (Liu et al., 2021). Sequencing libraries were generated, sequenced and bioinformatically analyzed as described in the ATACseq section.

For data processing, Trim Galore v. 0.4.4 (Kechin et al., 2017) (https://www.bioinformatics.babraham.ac.uk/projects/trim_galore/ ; accessed on 13 December 2020) was applied together with Cutadapt v. 1.14 (Martin, 2011) using "–paired", "–nextera", "– length_1 35", and "–length_2 35" parameters. Trimmed reads were mapped against the Genome Reference Consortium Human Build version 37 by means of Bowtie2 v. 2.2.6 (Langmead and Salzberg, 2012) using the "–very-sensitive" flag and a maximum insertion length of 2500 bp. Mappings belonging to the same lane-multiplexed library were combined using SAMtools merge v. 1.5 (Li et al., 2009). Discordant alignments and mappings with a Phred score below 20 were removed using SAMtools (Adey and Shendure, 2012), as fragments obtained from tagmentation cannot be smaller than 38 bp. Thus, all alignments corresponding to fragment sizes below that threshold were removed. Read ends were shifted to represent the center of the transposition event as previously described by (Buenrostro et al., 2013). Additionally, trimmed reads were aligned against the Saccharomyces cerevisiae R64 reference genome followed by post-alignment filtering as described above. To calculate a library-specific

scaling factor, we derived the multiplicative inverse of the number of filtered reads mapped to the yeast Cancers 2021, 13, 2455 9 of 26 genome. Coverage tracks were generated by means of the bamCoverage functionality of Deeptools v. 3.1.1 (Ramírez et al., 2016) using the non-default parameters "–ignoreForNormalization chrM chrY chrX" and "–effectiveGenomeSize 2652783500" as well as the "–scaleRatio" option to specify the spike-in-based scaling factor. The analysis procedure was implemented as fully containerized workflow using the Common Workflow Language v. 1.0. Differentially bound regions were identified as described for the ATACseq data.

Chromatin immunoprecipitation (ChIP):

ChIP assays were performed using iDeal ChIP-qPCR kit (C01010180, Diagenode). Cells were subject to fixation and crosslinking by formaldehyde (net concentration 1%) for 10-15 minutes at RT. Formaldehyde fixation is quenched by adding Glycine 125uM and incubating the fixed cellular suspension at RT for 5-10 minutes. The pellet is then washed twice by cold PBS and subjected then to lysis according to the specifications of the manufacturer. Next, cell lysates is subjected to sonication using bioruptor for 20 minutes (30 second ON/ 30 seconds OFF), so that the sheared smear is supposed to range from 200-600 bp long. The sheared chromatin is then subject for immunoprecipitation using high quality ChIP-grade antibodies against: HA (cell signaling), H3K27me3 (Diagenode), H3K4me3 (Diagenode), and polyclonal rabbit anti-IgG (c15410206, Diagenode) as negative control. Immunoprecipitation relies on that each antibody is crosslinked to protein A/G-coated magnetic beads, and the reaction takes up to 16 hours at 4°C, and then the beads crosslinked with the antibody-DNA is then subject for washing by buffers containing gradient concentrations of detergent. The washed beads-antibody-DNA is then subjected for de-crosslinking in the presence of proteinase K, so that all DNA-binding proteins, histones and beads are released, and the DNA sequences are then eluted and used for

downstream ChIP-real time PCR. The final eluted DNA was analyzed by real-time quantitative PCR with the Power SYBR Green PCR master mix (Applied Biosystems). The PCR conditions were: 50 °C for 2 min, 95 °C for 10 min, and 40 cycles of 95 °C for 15 s and 60 °C for 1 min. The PCR analysis was performed with the 7900HT fast real-time PCR system instrument and software (Applied Biosystems). All primers used to amplify the genomic target sites were designed by using PRIMER3 PLUS online tools. Primer sequences are listed in Supplement table 2.

The calculation of enrichment was normalized to the respective inputs and done according to the following formulas:

• The % of IP to input formula: % recovery = 2^[(Ct input-log2(5%)) – Ct sample] * 100%

• The enrichment was calculated as: %recovery IP / % recovery IgG

SAH concentration

Intracellular metabolites were isolated after lysating the cells in modified ripa buffer. Cell lysate was subjected to sonication using bioruptor for 5 minutes (30 second ON/ 30 seconds OFF). Resultant free cell supernatant was snap frozen and stored at -80 °C. Protein concentrations were determined using BCA (Pierce Biotechnology, Rockford, IL) and equal amounts of protein were used for SAH quantification. Quantification of intracellular SAH was done using S-Adenosylmethionine (SAM) and S-Adenosylhomocysteine (SAH) ELISA Combo Kit # MET-5151-C (Cell biolabs, San Diego, CA, USA) as instructed.

Methionine concentration:

Amino acid quantification was done at the Swedish Metabolomics Centre, Umeå, Sweden by LC-MSMS. This was done as following:

Standards and Calibration Curve

Aminoacid standards (alanine, arginine, aspartic acid, cysteine, glutamic acid, glycine, histidine, isoleucine, leucine, lysine, methionine, phenylalanine, proline, serine, threonine, tyrosine, valine, glutamine, asparagine, GABA, citrulline, ornithine, taurine, tryphtophan, 5-HTP and kynurenine) were purchased from Sigma (St. Louis, MO, USA). Isotopically labeled amino acid standards (alanine ($^{13}C_3$, ^{15}N), arginine ($^{13}C_6$, $^{15}N_4$), aspartic acid ($^{13}C_4$, ^{15}N), cystine ($^{13}C_6$, $^{15}N_2$), glutamic acid ($^{13}C_5$, ^{15}N), glycine ($^{13}C_2$, ^{15}N), histidine ($^{13}C_6$, $^{15}N_3$), isoleucine ($^{13}C_6$, ^{15}N), leucine ($^{13}C_6$, ^{15}N), lysine ($^{13}C_6$, $^{15}N_2$), methionine ($^{13}C_5$, ^{15}N), phenylalanine ($^{13}C_9$, ^{15}N), proline ($^{13}C_5$, ^{15}N), serine ($^{13}C_3$, ^{15}N), threonine ($^{13}C_4$, ^{15}N), tyrosine ($^{13}C_9$, ^{15}N), valine ($^{13}C_5$, ^{15}N), Citrulline (d4), GABA ($^{13}C_4$), glutamine ($^{13}C_5$), asparagine($^{13}C_4$), ornithine (d6), tryptophan (d8), kynurenine (d4)) were obtained from Cambridge Isotope Laboratories (Andover, MA). Stock solutions of each compound were prepared at a concentration of 500 ng/µL and stored at -80ºC. A 10-point calibration curve (0.01-100 pmol/µL) was prepared by serial dilutions and spiked with internal standards at a final concentration of 5 pmol/µL. Mass spectrometry grade formic acid was purchased from Sigma-Aldrich (St Louis, MO, USA) and HPLC grade acetonitrile from Fisher Scientific (Fair Lawn, NJ, USA). T

Amino acid extraction

One million cells were extracted with 400µL 90:10 (v/v) Methanol:water solution containing internal standards at 2.5 nmol/µL. One tungsten bead were added and the samples were shaken at 30 Hz for 2 min in a mixer mill. After removing the bead, the samples were centrifuged at 4 °C, 14000 RPM, for 10 min. The supernatant collected and stored at -80 °C until analysis.

Amino acid derivatization with AccQ-Tag

Extracted samples were derivatized by AccQ-Tag™ (Waters, Milford, MA, USA) according to the manufacturer's instructions. Briefly, 10 µL of extract were added to 70 µL of AccQ•Tag

Ultra Borate buffer and finally 20 µL of the freshly prepared AccQ•Tag derivatization solution was added, and the sample was immediately vortex for 30s.

Samples were kept at room temperature for 30 minutes followed by 10 minutes at 55ºC. For each batch quality control samples and procedure blanks were included.

Calibration curves were prepared in a similar way by adding 10 µL of each point of the curve to 70 µL of AccQ•Tag Ultra Borate buffer and 20 µL of the freshly prepared AccQ•Tag derivatization solution.

Amino acids Quantification by LC-ESI-MSMS

Derivatized solutions were analyzed using a 1290 Infinitely system from Agilent Technologies (Waldbronn, Germany), consisting G4220A binary pump, G1316C thermostated column compartment and G4226A autosampler with G1330B autosampler thermostat coupled to an Agilent 6460 triple quadrupole mass spectrometer equipped with a jet stream electrospray source operating in positive ion mode.

Separation was achieved injecting 1 µL of each sample onto a BEH C_{18} 2.1x100 mm, 1.7 µm column (Waters, Milford, MA, USA) held at 50ºC in a column oven. The gradient eluents used were H_2O 0.1% formic acid (A) and acetonitrile 0.1% formic acid (B) with a flow rate of 500 µL/min. The initial conditions consisted of 0% B, and the following gradient was used with linear increments: 0.54-3.50 minutes (0.1-9.1% B), 3.50-7.0 (9.1-17.0% B), 7.0-8.0 (17.0-19.70% B), 8.0-8.5 (19.7% B), 8.5-9.0 (19.7-21.2% B), 9.0-10.0 (21.2-59.6% B), 10.0-11.0 (59.6-95.0% B), 11.0-11.5 (95.0% B), 11.5-15.0 (0% B). From 13.0 minutes to 14.8 minutes the flow rate was set at 800 µL/min for a faster equilibration of the column.

The MS parameters were optimized for each compound as described in Supporting Information. MRM transitions for the derivatized amino acids were optimized using MassHunter MS Optimizer software (Agilent Technologies Inc., Santa Clara, CA, USA). The

fragmentor voltage was set at 380 V, the cell accelerator voltage at 7 V and the collision energies from 14-45V, nitrogen was used as collision gas. Jet-stream gas temperature was 290°C with a gas flow of 11 L/min, sheath gas temperature 325°C, sheath gas flow of 12 L/min. The nebulizer pressure was set to 20 psi and the capillary voltage was set at 4 kV. The QqQ was run in Dynamic MRM Mode with 2 min retention time windows and 500 msec cycle scans.

The data was quantified using MassHunter™ Quantitation software B08.00 (Agilent Technologies Inc., Santa Clara, CA, USA) and the amount of each amino acid was calculated based on the calibration curves.

Retention times (rt), MRM-transition stages monitored (precursor ion and product ions) and collision energies of analyzed compounds.

Compounds	MRM transition		rt (min)	Collision Energy (V)
	Precursor Ion	Product Ion		
alanine	260.1	171	4.1	14
arginine	345.1	171	2.8	35
aspartic acid	304.1	171	3.4	18
cystine	581	171	5.2	25
glutamic acid	318.1	171	3.6	22
glycine	246.1	171	3.1	18
histidine	326.1	171	2.6	26
isoleucine	302.1	171	7.8	18
leucine	302.1	171	7.6	18
lysine	487.2	171	5.1	26
methionine	320.1	171	6.0	22
phenylalanine	336.1	171	8.1	18
proline	286.1	171	4.4	14
serine	276.1	171	3.1	14
threonine	290.1	171	3.7	18
tyrosine	352.1	171	5.7	18

valine	288.1	171	6.1	18
citrulline	346.2	171	3.4	30
GABA	274.1	171	4.1	18
glutamine	317.1	171	3.0	22
asparagine	303.1	171	2.8	18
ornithine	473.2	171	4.7	34
tryptophan	375.2	171	8.4	26
kynurenin	379.2	171	7.6	37
Labelled internal standards				
alanine (13C3, 15N)	264.07	171	4.1	14
arginine (13C6, 15N4)	355.1	171	2.8	35
aspartic acid (13C4, 15N)	309.07	171	3.3	18
cystine (13C6, 15N2)	589	171	5.2	25
glutamic acid (13C5, 15N)	324.09	171	3.5	22
glycine (13C2, 15N)	249.05	171	3.1	18
histidine (13C6, 15N3)	335	171	2.6	26
isoleucine (13C6, 15N)	309.12	171	7.9	18
leucine (13C6, 15N)	309.12	171	7.6	18
lysine (13C6, 15N2)	495.1	171	5.2	26
methionine (13C5, 15N)	326.17	171	6.0	22
phenylalanine (13C9, 15N)	346	171	8.2	18
proline (13C5, 15N)	292.09	171	4.4	14
serine (13C3, 15N)	280.6	171	3.0	14
threonine (13C4, 15N)	295.08	171	3.7	18
tyrosine (13C9, 15N)	362.12	171	5.7	18
valine (13C5, 15N)	294.1	171	6.1	18
Citrulline (d4)	350.1	171	3.4	30
GABA (13C4)	278.1	171	4.0	18
glutamine (13C5)	322.1	171	3.1	22
asparagine(13C4)	307.1	171	2.8	18
ornithine (d6)	479	171	4.6	34
tryptophan (d8)	383.2	171	8.3	26

kynurenine (d4)	383	171	7.7	37

Statistical analysis

Two-sided Student's t-test were used for comparisons between different groups in all experiments. Log-rank test was used to compare survival between mice groups.

ACKNOWLEDGMENT

We thank Mohamad Ali and Akram Mendez for help with bioinformatic analysis. Tova Johansson and Hanna Brissman for help with animals. This work was supported by grants from the Swedish Cancer Society (CAN2017/461), the Swedish Childhood Cancer Foundation (PR2014-0125, PR2019-0013 and TJ2019-0053, TJ2022-0017), Wilhelm och Martina Lundgrens Fond, Assar Gabrielsson Fond and Västra Götalandsregionen (ALFGBG-431881). The computations were enabled by resources in project [SNIC 2021/22-754] provided by the Swedish National Infrastructure for Computing (SNIC) at UPPMAX, partially funded by the Swedish Research Council through grant agreement no. 2018-05973″. Proteomic analysis was preformed at the proteomics core facility of Sahlgrenska Academy, University of Gothenburg.

LP, AÖ and AW designed the research study. AW, AÖ, TN, DW, PL, JH, JA, SL, MHM performed laboratory work and result analysis. AW, LF, CP and LP analyzed the combined data and wrote the paper.

Conflict of interest

The authors declare no conflict of interest associated with this paper.

Data Availability Statement

The data that support the findings of this study are available in the supplementary material of this article, from Gene Expression Omnibus (GEO) database, accession number GSE182168, GSE202137 and GSE205698 and from PRIDE/ProteomeXchange, accession number PDXD034416. Further details and other data that support the findings of this study are available from the corresponding author upon request.

Ethics Statement

All animal experiments have been accepted by the Jordbruksverket and the animal ethics committee in Gothenburg, Dnr 5.8.18-17008/2021.

Reference List

Adey, A., and Shendure, J. (2012). Ultra-low-input, tagmentation-based whole-genome bisulfite sequencing. Genome Res *22*, 1139-1143.

Arabanian, L. S., Johansson, P., Staffas, A., Nilsson, T., Rouhi, A., Fogelstrand, L., and Palmqvist, L. (2018). The endothelin receptor type A is a downstream target of Hoxa9 and Meis1 in acute myeloid leukemia. Leuk Res *75*, 61-68.

Beerman, I., Bhattacharya, D., Zandi, S., Sigvardsson, M., Weissman, I. L., Bryder, D., and Rossi, D. J. (2010). Functionally distinct hematopoietic stem cells modulate hematopoietic lineage potential during aging by a mechanism of clonal expansion. Proc Natl Acad Sci U S A *107*, 5465-5470.

Berest, I., Arnold, C., Reyes-Palomares, A., Palla, G., Rasmussen, K. D., Giles, H., Bruch, P. M., Huber, W., Dietrich, S., Helin, K., and Zaugg, J. B. (2019). Quantification of Differential Transcription Factor Activity and Multiomics-Based Classification into Activators and Repressors: diffTF. Cell Rep *29*, 3147-3159 e3112.

Beverloo, H. B., Panagopoulos, I., Isaksson, M., van Wering, E., van Drunen, E., de Klein, A., Johansson, B., and Slater, R. (2001). Fusion of the homeobox gene HLXB9 and the ETV6 gene in infant acute myeloid leukemias with the t(7;12)(q36;p13). Cancer Res *61*, 5374-5377.

Biechonski, S., Yassin, M., and Milyavsky, M. (2017). DNA-damage response in hematopoietic stem cells: an evolutionary trade-off between blood regeneration and leukemia suppression. Carcinogenesis *38*, 367-377.

Bolouri, H., Farrar, J. E., Triche, T., Jr., Ries, R. E., Lim, E. L., Alonzo, T. A., Ma, Y., Moore, R., Mungall, A. J., Marra, M. A.*, et al.* (2018). The molecular landscape of pediatric acute myeloid leukemia reveals recurrent structural alterations and age-specific mutational interactions. Nature medicine *24*, 103-112.

Bowie, M. B., Kent, D. G., Dykstra, B., McKnight, K. D., McCaffrey, L., Hoodless, P. A., and Eaves, C. J. (2007). Identification of a new intrinsically timed developmental checkpoint that reprograms key hematopoietic stem cell properties. Proc Natl Acad Sci U S A *104*, 5878-5882.

Buenrostro, J. D., Giresi, P. G., Zaba, L. C., Chang, H. Y., and Greenleaf, W. J. (2013). Transposition of native chromatin for fast and sensitive epigenomic profiling of open chromatin, DNA-binding proteins and nucleosome position. Nature Methods *10*, 1213-1218.

Carter, B., Ku, W. L., Kang, J. Y., Hu, G., Perrie, J., Tang, Q., and Zhao, K. (2019). Mapping histone modifications in low cell number and single cells using antibody-guided chromatin tagmentation (ACT-seq). Nat Commun *10*, 3747.

Chen, C., Yu, W., Tober, J., Gao, P., He, B., Lee, K., Trieu, T., Blobel, G. A., Speck, N. A., and Tan, K. (2019). Spatial Genome Re-organization between Fetal and Adult Hematopoietic Stem Cells. Cell Rep *29*, 4200-4211 e4207.

Cho, R. H., Sieburg, H. B., and Muller-Sieburg, C. E. (2008). A new mechanism for the aging of hematopoietic stem cells: aging changes the clonal composition of the stem cell compartment but not individual stem cells. Blood *111*, 5553-5561.

Copley, M. R., and Eaves, C. J. (2013). Developmental changes in hematopoietic stem cell properties. Exp Mol Med *45*, e55.

Corces, M. R., Trevino, A. E., Hamilton, E. G., Greenside, P. G., Sinnott-Armstrong, N. A., Vesuna, S., Satpathy, A. T., Rubin, A. J., Montine, K. S., Wu, B.*, et al.* (2017). An improved ATAC-seq protocol reduces background and enables interrogation of frozen tissues. Nat Methods *14*, 959-962.

Couture, J. F., Hauk, G., Thompson, M. J., Blackburn, G. M., and Trievel, R. C. (2006). Catalytic roles for carbon-oxygen hydrogen bonding in SET domain lysine methyltransferases. J Biol Chem *281*, 19280-19287.

Dalgin, G., Ward, A. B., Hao le, T., Beattie, C. E., Nechiporuk, A., and Prince, V. E. (2011). Zebrafish mnx1 controls cell fate choice in the developing endocrine pancreas. Development *138*, 4597-4608.
De Braekeleer, E., Douet-Guilbert, N., Morel, F., Le Bris, M. J., Basinko, A., and De Braekeleer, M. (2012). ETV6 fusion genes in hematological malignancies: a review. Leuk Res *36*, 945-961.
Detich, N., Hamm, S., Just, G., Knox, J. D., and Szyf, M. (2003). The methyl donor S-Adenosylmethionine inhibits active demethylation of DNA: a candidate novel mechanism for the pharmacological effects of S-Adenosylmethionine. J Biol Chem *278*, 20812-20820.
Espersen, A. D. L., Noren-Nystrom, U., Abrahamsson, J., Ha, S. Y., Pronk, C. J., Jahnukainen, K., Jonsson, O. G., Lausen, B., Palle, J., Zeller, B.*, et al.* (2018). Acute myeloid leukemia (AML) with t(7;12)(q36;p13) is associated with infancy and trisomy 19: Data from Nordic Society for Pediatric Hematology and Oncology (NOPHO-AML) and review of the literature. Genes, chromosomes & cancer *57*, 359-365.
Fuller, R. W., and Nagarajan, R. (1978). Inhibition of methyltransferases by some new analogs of S-adenosylhomocysteine. Biochem Pharmacol *27*, 1981-1983.
Golub, T. R., Barker, G. F., Lovett, M., and Gilliland, D. G. (1994). Fusion of PDGF receptor beta to a novel ets-like gene, tel, in chronic myelomonocytic leukemia with t(5;12) chromosomal translocation. Cell *77*, 307-316.
Harrison, K. A., Thaler, J., Pfaff, S. L., Gu, H., and Kehrl, J. H. (1999). Pancreas dorsal lobe agenesis and abnormal islets of Langerhans in Hlxb9-deficient mice. Nat Genet *23*, 71-75.
Hey, J., Paulsen, M., Toth, R., Weichenhan, D., Butz, S., Schatterny, J., Liebers, R., Lutsik, P., Plass, C., and Mall, M. A. (2021). Epigenetic reprogramming of airway macrophages promotes polarization and inflammation in muco-obstructive lung disease. Nat Commun *12*, 6520.
Hock, H., Meade, E., Medeiros, S., Schindler, J. W., Valk, P. J., Fujiwara, Y., and Orkin, S. H. (2004). Tel/Etv6 is an essential and selective regulator of adult hematopoietic stem cell survival. Genes & development *18*, 2336-2341.
Hock, H., and Shimamura, A. (2017). ETV6 in hematopoiesis and leukemia predisposition. Semin Hematol *54*, 98-104.
Inomata, K., Aoto, T., Binh, N. T., Okamoto, N., Tanimura, S., Wakayama, T., Iseki, S., Hara, E., Masunaga, T., Shimizu, H., and Nishimura, E. K. (2009). Genotoxic stress abrogates renewal of melanocyte stem cells by triggering their differentiation. Cell *137*, 1088-1099.
Jacob, Y., and Voigt, P. (2018). In Vitro Assays to Measure Histone Methyltransferase Activity Using Different Chromatin Substrates. Methods Mol Biol *1675*, 345-360.
Kaiser, P. (2020). Methionine Dependence of Cancer. Biomolecules *10*.
Kechin, A., Boyarskikh, U., Kel, A., and Filipenko, M. (2017). cutPrimers: A New Tool for Accurate Cutting of Primers from Reads of Targeted Next Generation Sequencing. J Comput Biol *24*, 1138-1143.
Kogan, S. C., Ward, J. M., Anver, M. R., Berman, J. J., Brayton, C., Cardiff, R. D., Carter, J. S., de Coronado, S., Downing, J. R., Fredrickson, T. N.*, et al.* (2002). Bethesda proposals for classification of nonlymphoid hematopoietic neoplasms in mice. Blood *100*, 238-245.
Kulakovskiy, I. V., Vorontsov, I. E., Yevshin, I. S., Sharipov, R. N., Fedorova, A. D., Rumynskiy, E. I., Medvedeva, Y. A., Magana-Mora, A., Bajic, V. B., Papatsenko, D. A.*, et al.* (2018). HOCOMOCO: towards a complete collection of transcription factor binding models for human and mouse via large-scale ChIP-Seq analysis. Nucleic Acids Res *46*, D252-D259.
Lagunas-Rangel, F. A., Chavez-Valencia, V., Gomez-Guijosa, M. A., and Cortes-Penagos, C. (2017). Acute Myeloid Leukemia-Genetic Alterations and Their Clinical Prognosis. Int J Hematol Oncol Stem Cell Res *11*, 328-339.
Langmead, B., and Salzberg, S. L. (2012). Fast gapped-read alignment with Bowtie 2. Nature Methods *9*, 357-359.
Leotta, C. G., Federico, C., Brundo, M. V., Tosi, S., and Saccone, S. (2014). HLXB9 gene expression, and nuclear location during in vitro neuronal differentiation in the SK-N-BE neuroblastoma cell line. PLoS One *9*, e105481.
Li, H., Arber, S., Jessell, T. M., and Edlund, H. (1999). Selective agenesis of the dorsal pancreas in mice lacking homeobox gene Hlxb9. Nature genetics *23*, 67-70.

Li, H., Handsaker, B., Wysoker, A., Fennell, T., Ruan, J., Homer, N., Marth, G., Abecasis, G., and Durbin, R. (2009). The Sequence Alignment/Map format and SAMtools. Bioinformatics *25*, 2078-2079.
Liu, C. S., Toth, R., Bakr, A., Goyal, A., Islam, M. S., Breuer, K., Mayakonda, A., Lin, Y. Y., Stepper, P., Jurkowski, T. P.*, et al.* (2021). Epigenetic Modulation of Radiation-Induced Diacylglycerol Kinase Alpha Expression Prevents Pro-Fibrotic Fibroblast Response. Cancers (Basel) *13*.
Love, M. I., Huber, W., and Anders, S. (2014). Moderated estimation of fold change and dispersion for RNA-seq data with DESeq2. Genome Biol *15*, 550.
Mandal, P. K., and Rossi, D. J. (2012). DNA-damage-induced differentiation in hematopoietic stem cells. Cell *148*, 847-848.
Manesia, J. K., Xu, Z., Broekaert, D., Boon, R., van Vliet, A., Eelen, G., Vanwelden, T., Stegen, S., Van Gastel, N., Pascual-Montano, A.*, et al.* (2015). Highly proliferative primitive fetal liver hematopoietic stem cells are fueled by oxidative metabolic pathways. Stem Cell Res *15*, 715-721.
Martin, M. (2011). Cutadapt removes adapter sequences from high-throughput sequencing reads. EMBnetjournal *17*.
McIntosh, B. E., and Brown, M. E. (2015). No irradiation required: The future of humanized immune system modeling in murine hosts. Chimerism *6*, 40-45.
Nilsson, T., Waraky, A., Ostlund, A., Li, S., Staffas, A., Asp, J., Fogelstrand, L., Abrahamsson, J., and Palmqvist, L. (2022). An induced pluripotent stem cell t(7;12)(q36;p13) acute myeloid leukemia model shows high expression of MNX1 and a block in differentiation of the erythroid and megakaryocytic lineages. Int J Cancer.
Pan, Y. R., and Lee, E. Y. (2009). UV-dependent interaction between Cep164 and XPA mediates localization of Cep164 at sites of DNA damage and UV sensitivity. Cell Cycle *8*, 655-664.
Parkhitko, A. A., Jouandin, P., Mohr, S. E., and Perrimon, N. (2019). Methionine metabolism and methyltransferases in the regulation of aging and lifespan extension across species. Aging Cell *18*, e13034.
Picelli, S., Bjorklund, A. K., Reinius, B., Sagasser, S., Winberg, G., and Sandberg, R. (2014). Tn5 transposase and tagmentation procedures for massively scaled sequencing projects. Genome Res *24*, 2033-2040.
Ramírez, F., Ryan, D. P., Grüning, B., Bhardwaj, V., Kilpert, F., Richter, A. S., Heyne, S., Dündar, F., and Manke, T. (2016). deepTools2: a next generation web server for deep-sequencing data analysis. Nucleic Acids Research *44*, W160-W165.
Rawat, V. P., Cusan, M., Deshpande, A., Hiddemann, W., Quintanilla-Martinez, L., Humphries, R. K., Bohlander, S. K., Feuring-Buske, M., and Buske, C. (2004). Ectopic expression of the homeobox gene Cdx2 is the transforming event in a mouse model of t(12;13)(p13;q12) acute myeloid leukemia. Proc Natl Acad Sci U S A *101*, 817-822.
Robinson, M. D., McCarthy, D. J., and Smyth, G. K. (2010). edgeR: a Bioconductor package for differential expression analysis of digital gene expression data. Bioinformatics *26*, 139-140.
Ross-Innes, C. S., Stark, R., Teschendorff, A. E., Holmes, K. A., Ali, H. R., Dunning, M. J., Brown, G. D., Gojis, O., Ellis, I. O., Green, A. R.*, et al.* (2012). Differential oestrogen receptor binding is associated with clinical outcome in breast cancer. Nature *481*, 389-393.
Ross, A. J., Ruiz-Perez, V., Wang, Y., Hagan, D. M., Scherer, S., Lynch, S. A., Lindsay, S., Custard, E., Belloni, E., Wilson, D. I.*, et al.* (1998). A homeobox gene, HLXB9, is the major locus for dominantly inherited sacral agenesis. Nat Genet *20*, 358-361.
Sanderson, S. M., Gao, X., Dai, Z., and Locasale, J. W. (2019). Methionine metabolism in health and cancer: a nexus of diet and precision medicine. Nat Rev Cancer *19*, 625-637.
Scheffold, A., Baig, A. H., Chen, Z., von Lohneysen, S. E., Becker, F., Morita, Y., Avila, A. I., Groth, M., Lechel, A., Schmid, F.*, et al.* (2020). Elevated Hedgehog activity contributes to attenuated DNA damage responses in aged hematopoietic cells. Leukemia *34*, 1125-1134.
Schneider, C. A., Rasband, W. S., and Eliceiri, K. W. (2012). NIH Image to ImageJ: 25 years of image analysis. Nat Methods *9*, 671-675.

Sivasubramaniam, S., Sun, X., Pan, Y. R., Wang, S., and Lee, E. Y. (2008). Cep164 is a mediator protein required for the maintenance of genomic stability through modulation of MDC1, RPA, and CHK1. Genes Dev *22*, 587-600.
Sun, M.-a., Ralls, S., Wu, W., Demmerle, J., Jiang, J., Miller, C., Wolf, G., and Macfarlan, T. S. (2021). Homeobox transcription factor MNX1 is crucial for restraining the expression of pan-neuronal genes in motor neurons. bioRxiv, 2021.2008.2007.455331.
Thaler, J., Harrison, K., Sharma, K., Lettieri, K., Kehrl, J., and Pfaff, S. L. (1999). Active suppression of interneuron programs within developing motor neurons revealed by analysis of homeodomain factor HB9. Neuron *23*, 675-687.
Tosi, S., Mostafa Kamel, Y., Owoka, T., Federico, C., Truong, T. H., and Saccone, S. (2015). Paediatric acute myeloid leukaemia with the t(7;12)(q36;p13) rearrangement: a review of the biological and clinical management aspects. Biomark Res *3*, 21.
von Bergh, A. R., van Drunen, E., van Wering, E. R., van Zutven, L. J., Hainmann, I., Lonnerholm, G., Meijerink, J. P., Pieters, R., and Beverloo, H. B. (2006). High incidence of t(7;12)(q36;p13) in infant AML but not in infant ALL, with a dismal outcome and ectopic expression of HLXB9. Genes Chromosomes Cancer *45*, 731-739.
Wang, J., and Abate-Shen, C. (2012). The MSX1 homeoprotein recruits G9a methyltransferase to repressed target genes in myoblast cells. PLoS One *7*, e37647.
Wang, J., Kumar, R. M., Biggs, V. J., Lee, H., Chen, Y., Kagey, M. H., Young, R. A., and Abate-Shen, C. (2011). The Msx1 Homeoprotein Recruits Polycomb to the Nuclear Periphery during Development. Dev Cell *21*, 575-588.
Waraky, A., Akopyan, K., Parrow, V., Stromberg, T., Axelson, M., Abrahmsen, L., Lindqvist, A., Larsson, O., and Aleem, E. (2014). Picropodophyllin causes mitotic arrest and catastrophe by depolymerizing microtubules via insulin-like growth factor-1 receptor-independent mechanism. Oncotarget *5*, 8379-8392.
Waraky, A., Lin, Y., Warsito, D., Haglund, F., Aleem, E., and Larsson, O. (2017). Nuclear insulin-like growth factor 1 receptor phosphorylates proliferating cell nuclear antigen and rescues stalled replication forks after DNA damage. J Biol Chem *292*, 18227-18239.
Weichenhan, D., Wang, Q., Adey, A., Wolf, S., Shendure, J., Eils, R., and Plass, C. (2018). Tagmentation-Based Library Preparation for Low DNA Input Whole Genome Bisulfite Sequencing. Methods Mol Biol *1708*, 105-122.
Ye, C., Sutter, B. M., Wang, Y., Kuang, Z., Zhao, X., Yu, Y., and Tu, B. P. (2019). Demethylation of the Protein Phosphatase PP2A Promotes Demethylation of Histones to Enable Their Function as a Methyl Group Sink. Mol Cell *73*, 1115-1126 e1116.
Yu, G., Wang, L. G., and He, Q. Y. (2015). ChIPseeker: an R/Bioconductor package for ChIP peak annotation, comparison and visualization. Bioinformatics *31*, 2382-2383.
Zarou, M. M., Vazquez, A., and Vignir Helgason, G. (2021). Folate metabolism: a re-emerging therapeutic target in haematological cancers. Leukemia *35*, 1539-1551.
Zelent, A., Greaves, M., and Enver, T. (2004). Role of the TEL-AML1 fusion gene in the molecular pathogenesis of childhood acute lymphoblastic leukaemia. Oncogene *23*, 4275-4283.
Zhang, J., and Zheng, Y. G. (2016). SAM/SAH Analogs as Versatile Tools for SAM-Dependent Methyltransferases. ACS Chem Biol *11*, 583-597.
Zheng, Y., and Cantley, L. C. (2019). Toward a better understanding of folate metabolism in health and disease. J Exp Med *216*, 253-266.

FIGURE LEGENDS

Figure 1. MNX1 induce AML in immunocompromised mice. Kaplan-Meier survival curve of (NBSGW) mice transplanted with FL cells after retrovirus transduction with either ectopic expression of *MNX1* (green), *ETV6* (purple), *MNX1::ETV6* fusion (red) or empty vector Ctrl (blue). Results from the transplanted mice (control n = 11, *MNX1*: n = 12, *ETV6* and *MNX1::ETV6* n = 4) were analyzed using the log-rank test (***: significant at $P \leq 0.01$, ns: non-significant) (a). Mice were euthanized at the end of the experiment and analyzed for spleen weight, white blood cell number and hemoglobin concentration (b). Representative dot plots from the flow cytometry analysis for the bone marrow of the euthanized mice at the end of the experiment with the indicated antibodies (c and d). Data represent mean ± SD of at least three experiments and is considered significant using two sided student t-test (**) at $p \leq 0.01$ and (*) at $p \leq 0.05$, or non-significant (ns) at $p > 0.05$. Representative images of H and E-stained formaldehyde fixed spleen and liver sections from Ctrl and MNX1 mice (e; left-panels). Representative images of Giemsa-stained peripheral blood smears from Ctrl and MNX1 mice (e; right-panels) (e).

FL: Fetal liver, BM: bone marrow, Ctrl: control empty vector, Fusion: *MNX1::ETV6* fusion, HGB: Hemoglobin, LSK: $Lin^{-}Sca\text{-}1^{+}c\text{-}Kit^{+}$, NSG: NOD.Cg-$Kit^{W\text{-}41J}$ Tyr^{+} $Prkdc^{scid}$ $Il2rg^{tm1Wjl}$/ThomJ (NBSGW), HandE: hematoxylin and eosin.

Figure 2. MNX1 alters differentiation and proliferation of FL cells. Representative dot plots from the flow cytometry analysis of FL cells transduced with ectopic expression of *MNX1*, *ETV6*, *MNX1::ETV6* fusion or empty vector with the indicated antibodies (let panel, a-c). Blue population represents the positive population. Quantification of the flowcytometry analysis represented as percentage of population (right panel, a-c). CFU two weeks after

transduction of FL cells (d), or weekly number of colonies with relating for five weeks (e). MTT proliferation assay of transduced FL cells (f). Data represent mean ± SD of at least three experiments and is considered significant using two sided student t-test (**) at $p \leq 0.01$ and (*) at $p \leq 0.05$.

FL: fetal liver, Ctrl: control empty vector, Fusion: *MNX1::ETV6* fusion, LSK: $Lin^{-}Sca\text{-}1^{+}c\text{-}Kit^{+}$), lin+: lineage positive, CFU: colony forming unit, GM: granulocyte, macrophage, GEMM: granulocyte, erythroid, macrophage, megakaryocyte, BFU: Burst-forming unit.

Figure 3. Downstream targets of MNX1 overexpression. LogFC heat map of downregulated (blue) and upregulated (red) differentially expressed genes of leukemia BM cells with *MNX1* ectopic expression in comparison with FL cells with empty vector (Ctrl). Results were considered at the log fold-change cutoff (logFC) of ≥ |1| and false discovery rate (FDR) of ≤0.05 (a). PCA scatter plot of normalized gene expression using variance Stabilizing Transformation (b). Volcano plot of differentially expressed genes (c). Gene set enrichment analysis (GSEA) using the Gene ontology biological pathways (GO) gene set showing normalized enrichment score for pathways with NOM p-value ≤ 0.05 (d).

LogFC: Log fold change, PCA: principal component analysis, FL: fetal liver, BM: Bone marrow, Ctrl: control empty vector, Fusion: *MNX1::ETV6* fusion, NSG: NOD.Cg-$Kit^{W\text{-}41J}$ Tyr^{+} $Prkdc^{scid}$ $Il2rg^{tm1Wjl}$/ThomJ (NBSGW), PCA: principal component analysis, LogFC: Log fold change, FDR: false recovery date, ChIP: chromatin immunoprecipitation.

Figure 4. MNX1 induces DNA damage. Immunofluorescence of FL cells stained with γH2AX –FITC antibody (green) and counterstained with DAPI (blue) (left panel, a). Quantification of the number of γH2AX foci/cell. At least 50 cells were counted (right panel,

a). Representative histogram from the flow cytometry analysis of FL and ABM cells after staining with DAPI for cell cycle distribution (left panel, b). Quantification of the flowcytometry analysis represented as fold difference relative to control (right panel, b). Representative dot plots from the flow cytometry analysis of FL and ABM cells after double staining with Annexin/V and DAPI for apoptotic analysis (upper panel, c). Quantification of the flowcytometry analysis represented as fold difference relative to control (lower panel, c). Representative histogram from the flow cytometry analysis of BM from leukemia NBSGW mice transduced with MNX1-FL cells (yellow) in comparison with NBSGW mice transduced with empty vector Ctrl (red) after staining with DAPI for DNA content, numbers indicated median DNA values at G1 phase and G2 phase of cell cycle. (d). Quantification of DNA content in supplement figure 7c. Data represent mean ± SD of at least three experiments and is considered significant using two sided student t-test (**) at $p \leq 0.01$ and (*) at $p \leq 0.05$.

FL: fetal liver, ABM: adult bone marrow, Ctrl: control empty vector, Fusion: *MNX1::ETV6* fusion, e.A: early apoptosis, l.A: late apoptosis.

Figure 5. MNX1 alters histone methylation. mRNA expression of *Cep164* determined by quantitative real time qPCR, normalized to *Hprt* and represented as fold difference relative to control from both in vitro FL cells (MNX1-FL) and BM from leukemia mice (MNX1-BM) (a). Quantification of the binding of MNX1 to the promoter regions of *Cep164* in FL cells with either MNX1 of empty vector determined by ChIP-qPCR (b). Western blot analysis of H3K4me1, H3K4me2, H3K4me3 and H3K27me3 in the transduced FL cells. Histone 3 and actin used as loading controls (c). Heatmap of differentially bound H3K27me3 from BM of leukemic mice (MNX1) versus control FL cells transduced with empty vector (Ctrl) as determined by ACT-Seq (left panel, d). Annotation of different enriched regions for

H3K27me3 ACT-Seq (right panel, d). Results were considered at the log fold-change cutoff (logFC) of ≥ |1| and false discovery rate (FDR) of ≤0.05. Heatmap of differentially accessible regions from BM of leukemic mice (MNX1) versus control FL cells transduced with empty vector (Ctrl) as determined by ATAC-Seq (left panel, e). Annotation of different enriched regions for ATAC-Seq (right panel, e). Results were considered at the log fold-change cutoff (logFC) of ≥ |1| and false discovery rate (FDR) of ≤0.05. Pathway enrichment analysis for the identified proteins after Co-IP and mass spectrometry using STRING with reactome data set, showing strength of the pathway as Log10 observed proteins/background in the respective pathway (f). The binding of AHCY and MAT2A was detected by immunoprecipitation of MNX1 using HA-antibody followed by western blot using AHCY and MAT2A antibodies. ETV6 with HA tag was used as a negative control. Total protein input used as loading control (g). Methionine concentration was determined by LC-ESI-MSMS from Fl cells expressing MNX1 (MNX1-FL) and leukemia BM cells (MNX1-BM), normalized against total protein concentration and represented as fold difference relative to control (h). Recombinant Histone H3.1and H3.3 were subjected to an invitro methyltransferase reaction using MNX1 complex pulled down with HA antibody from FL cells transduced with MNX1(M), in comparison with FL cells with empty vector (C), in the presence of SAM and DTT. The reactions were terminated by boiling in SDS sample buffer. Separation of samples in 12% SDS-PAGE was followed by immunoblotting (IB) with mono, di and tri methyl-lysines antibody. Reblotting was made for detection of HA and total Histone H3. As indicated, negative controls were obtained by omitting Histone H3, or the pulled down immune complex (left panel, i). Quantification of the invitro methyltransferase reaction (right panel, i). Data represent mean ± SD of at least three experiments and is considered significant using two sided student t-test (**) at $p \leq 0.01$ and (*) at $p \leq 0.05$.

FL: fetal liver, BM: Bone marrow, Ctrl: control empty vector, Fusion: *MNX1::ETV6* fusion , WB: western blot, ChIP: chromatin immunoprecipitation, SAM: S-Adenosyl methionine , DTT: Dithiothreitol.

Figure 6. Sinefungin rescued MNX1 induced phenotype. Protein expression levels of H3K4me3, H3k27me3, H3K4me1 and H3K4me2 in Fl cells with either MNX1 overexpression or empty vector (ctrl) after treatment with vehicle or 5μM Sinefungin (Ctrl+S, MNX1+S) as determined by western blotting. Actin served as loading control (a). Quantification of the western blot analysis in supplement figure 9a. Quantification of the number of γH2AX foci/cell. At least 50 cells were counted. Data represented as fold difference relative to control (b). Quantification of flow cytometry analysis of the cells with the indicated antibodies. Data represented as fold difference relative to control (c and d). Data represent mean ± SD of at least three experiments and is considered significant using two sided student t-test (**) at $p \leq 0.01$ and (*) at $p \leq 0.05$. Kaplan-Meier survival curves of (NBSGW) mice transplanted with FL cells after retrovirus transduction with either ectopic expression of MNX1 or empty vector (Ctrl) after treatment with vehicle or 5μM Sinefungin (MNX1+S, Ctrl+S). Results of MNX1 (n = 7) and Sinefungin treated MNX1 cells (MNX1+S) (n = 6) were analyzed using the log-rank test (***: significant at $P \leq 0.01$) (e). Heatmap of sample distance and similarity matrix for the differentially expressed genes with either ectopic expression of MNX1 or empty vector (Ctrl) with or without 5μM Sinefungin (Ctrl+S, MNX1+S), showing clustering of cells and similarity between the samples. Results were considered at the log fold-change cutoff (LogFC) ≥ |1.5| and FDR ≤ 0.05 (f). Gene ontology (GO) go biological process pathways enrichment analysis for most significant pathways of the differentially expressed genes between the human t(7;12) IPSC model and MNX1 overexpression mouse model using the default parameters. Y-axis represent –log10 of the FDR adjusted p value (g, right panel). Venn diagram of the number of

common pathways determined from Gene ontology (GO) enrichment analysis between the human t(7;12) IPSC model and MNX1 overexpression mouse model (g, left panel). Schematic diagram for the proposed model of action of MNX1 (h).

Table 1. In-silico predicted transcription factor binding sites by DiffTF package from ATAC-Seq showing top differentially activated (FDR < 0.05) transcription factors (TFs) binding between MNX1 BM from leukemia mice and FL Ctrl cells

Up-regulated TFs	**weighted_mean Difference**	**pvalueAdj**	**Down regulated Tfs**	**weighted_mean Difference**	**pvalueAdj**
Tal1.a	1.294844532	9.30E-79	Fosl2	-0.421333369	1.84E-24
Gata1	0.567577232	1.24E-20	Jun	-0.415408916	2.58E-23
Gata3	0.550998432	1.12E-19	Cebpe	-0.39280302	0.000108
Gata2	0.540274293	1.01E-16	Batf	-0.387629056	1.57E-17
Alx1	0.371423122	0.023026	Fosl1	-0.384618862	4.57E-21
Nf2l2	0.288226747	2.11E-17	Cebpa	-0.353311343	3.14E-06
Zeb1	0.232871599	9.60E-41	Gfi1	-0.349686909	8.73E-08
Tbx5	0.231419764	1.76E-09	Fosb	-0.339609157	5.76E-15
Mafk.s	0.22701829	3.01E-10	Sta5a	-0.339203846	2.94E-09
Nfe2	0.218904994	4.77E-11	Jund	-0.337147615	8.92E-16
Gata6	0.213067314	2.28E-11	Cebpd	-0.323368792	0.000182
Foxo3	0.202788032	0.000274	Gfi1b	-0.308823273	8.94E-12

Table 2. Identified proteins in top enriched pathways after Co-IP of proteins in complex with MNX1 and mass spectrometry analysis. As determined by STRING using reactome data set

Pathway	**Matching proteins**
Association with TriC/CCT	Cct8,Cct6a,Tcp1,Cct4
Methylation	Mat2b,Ahcy,Mat2a,Trmt112
RHO GTPases activate PAKs	Ppp1cb,Myh9,Myh11,Myh10,Myh14
Citric acid cycle (TCA cycle)	Cs,Mdh2,Idh3g,Dld
Pyruvate metabolism	Pdk3,Slc16a3,Vdac1,Ldha,Dld
Actin dynamics for phagocytic	Actr2,Arpc2,Myh9,Cyfip2,Arpc3,Myo5a,Actr3
Translation initiation complex	Pabpc1,Eif3e,Rps21,Eif2s3x,Rps12,Rps28
RHO GTPase Effectors	Actr2,Mapk14,Arpc2,Ppp1cb,Myh9,Pfn1,Aurkb,S100a8,Tuba1b,Bub3,Myh11,Cyfip2,Arpc3,Myh10,Ywhaq,Myh14,Kif2a,S100a9,Actr3
Cellular Senescence	Mapk14,Asf1a,Lmnb1,Txn1,H2afz,Hist1h1b,Hist2h2be,Eed
Mitotic Anaphase	Psmd11,Aurkb,Psmd6,Lmnb1,Smc3,Psmd13,Chmp4b,Smc1a,Tuba1b,Rcc1,Bub3,Kif2a
M Phase	Psmd11,Aurkb,Psmd6,Lmnb1,Smc3,Psmd13,Chmp4b,H2afz,Smc1a,Smc4,Tuba1b,Rcc1,Bub3,Hist2h2be,Csnk2a1,Smc2,Kif2a
Metabolism of proteins	Pabpc1,Srp14,Psmd11,Rab10,Ddx5,Aurkb,Psmd6,Vdac2,Ero1l,Eif3e,Mrpl21,Smc3,Psmd13,Cct8,Srp9,Txn1,Trappc3,Cct6a,Cmas,Rab27a,Rpl22l1,Smc1a,Rpl37,Mat2b,Pdia6,Fn1,Rps21,Eif2s3x,Hist2h2ab,Rps12,Tuba1b,Ctbp1,Rpl15,Rpl36,Rpl34,Lgals1,Hist2h2be,Eef1g,Csnk2a1,Vdac1,Wdr5,Rps28,Trmt112,Tcp1,Copa,Gnb4,Ctsd,Cct4,Nop58,Tceb1
Metabolism of RNA	Pabpc1,U2af2,Psmd11,Prpf8,Snrpd3,Ddx5,Psmd6,Wdr46,Psmd13,Rpl22l1,Rpl37,Utp15,Wdr43,Rps21,Rcl1,Rps12,Rpl15,Rpl36,Rpl34,Srsf2,Nhp2l1,Snrpb,Rps28,Srsf3,Ddx6,Hnrnpd,Apobec3,Nop58

Table 3. LogFC values of Mat2a, Ahcy and Cep164 from RNA-Seq of leukemia BM from mice transplanted with ectopic expression of *MNX1* vs Fl cells with empty vector in comparison with RNA-Seq data from iPSC with t(7;12) and invitro FL cells pre-transplantation in mice

Gene name	**LogFC Leukemia BM vs Ctrl FL cells with empty vector**	**pvalue Adj**	**LogFC iPSC with t(7;12)**	**pvalue Adj**	**LogFC FL with MNX1 vs FL with empty vector**	**pvalue Adj**
Mat2a	0.906196	1.46E-09	0.22072695	0.01875	-0.53568	0.36647
Ahcy	0.252869	0.1	0.38072843	0.0007	-0.01931	0.9958
Cep164	3.352978	5.56E-75	1.38441255	7.36E-30	0.70794	0.05674

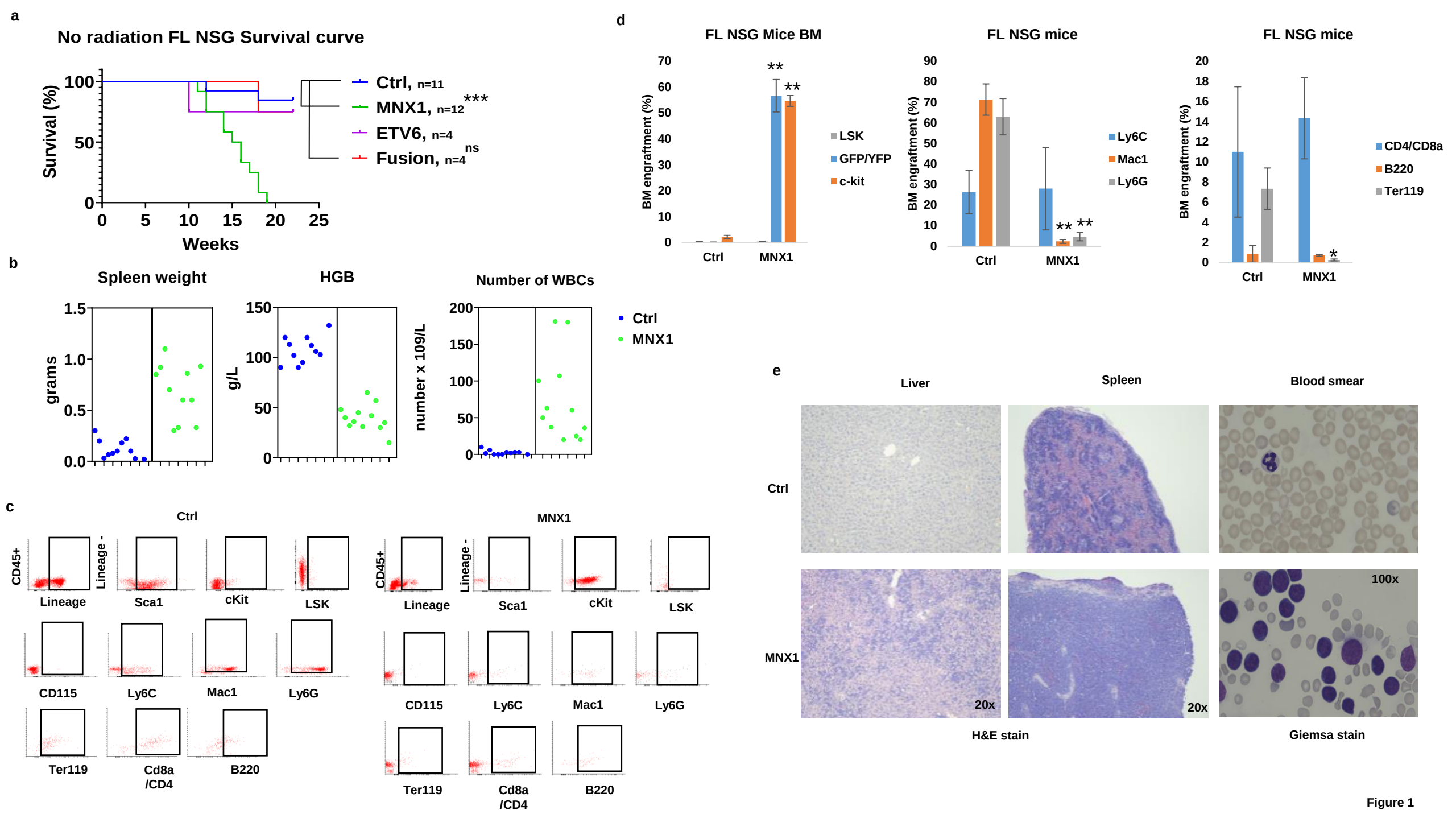
a
No radiation FL NSG Survival curve
Survival (%)
Weeks
Ctrl, n=11
MNX1, n=12
***
ETV6, n=4
Fusion, n=4
ns
b
Spleen weight
grams
HGB
g/L
Number of WBCs
number x 109/L
Ctrl
MNX1
c
Ctrl
MNX1
CD45+
Lineage -
Lineage
Sca1
cKit
LSK
CD115
Ly6C
Mac1
Ly6G
Ter119
Cd8a /CD4
B220
d
FL NSG Mice BM
BM engraftment (%)
LSK
GFP/YFP
c-kit
FL NSG mice
Ly6C
Mac1
Ly6G
CD4/CD8a
B220
Ter119
Ctrl
MNX1
e
Liver
Spleen
Blood smear
Ctrl
MNX1
20x
100x
H&E stain
Giemsa stain

Figure 1

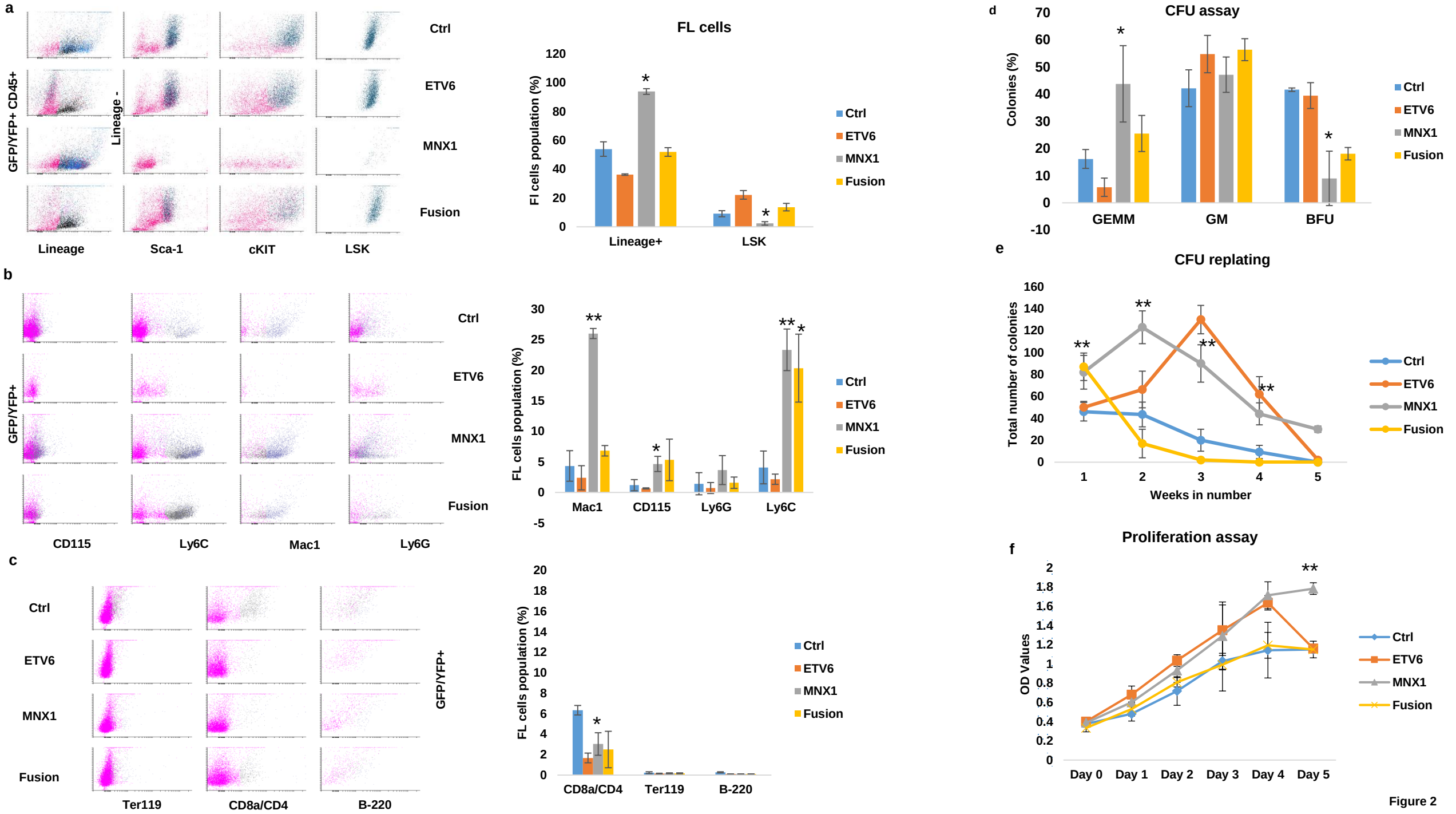
a
GFP/YFP+ CD45+
Lineage -
Ctrl
ETV6
MNX1
Fusion
Lineage
Sca-1
cKIT
LSK
FL cells
Fl cells population (%)
Lineage+
LSK
Ctrl
ETV6
MNX1
Fusion
b
GFP/YFP+
CD115
Ly6C
Mac1
Ly6G
FL cells population (%)
Mac1
CD115
Ly6G
Ly6C
c
GFP/YFP+
Ter119
CD8a/CD4
B-220
FL cells population (%)
d
CFU assay
Colonies (%)
GEMM
GM
BFU
e
CFU replating
Total number of colonies
Weeks in number
f
Proliferation assay
OD Values
Day 0
Day 1
Day 2
Day 3
Day 4
Day 5

Figure 2

a

Heatmap of RNA-seq from BM of NSG mice.
LogFC 1 and FDR ≤ 0.05

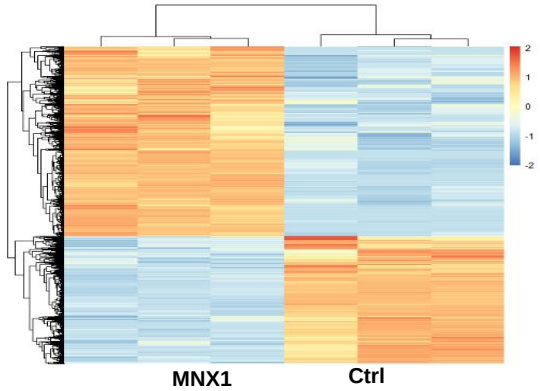

b

PCA of RNA-seq from BM of NSG mice

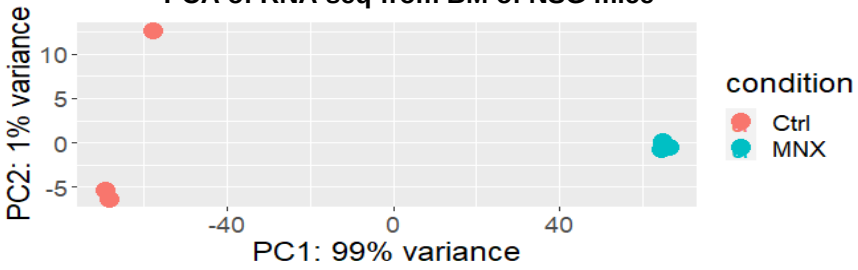

c

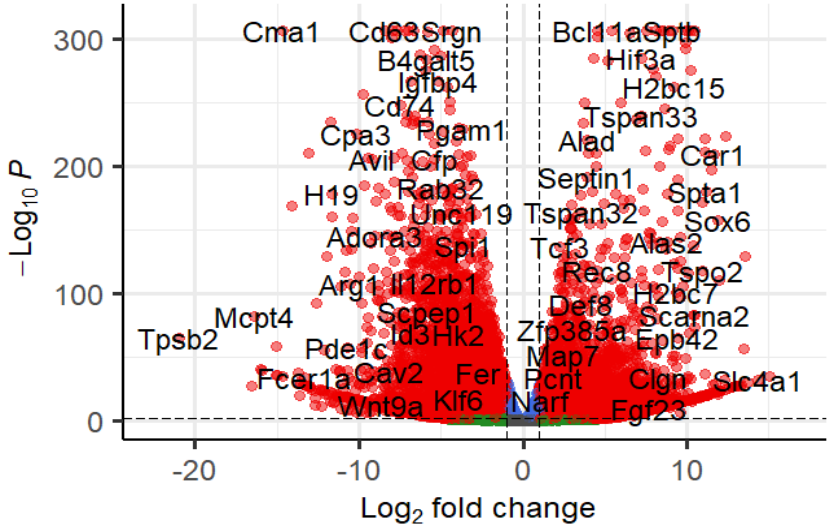

d

Gene enrichment analysis of RNA-Seq using Gene ontology gene set

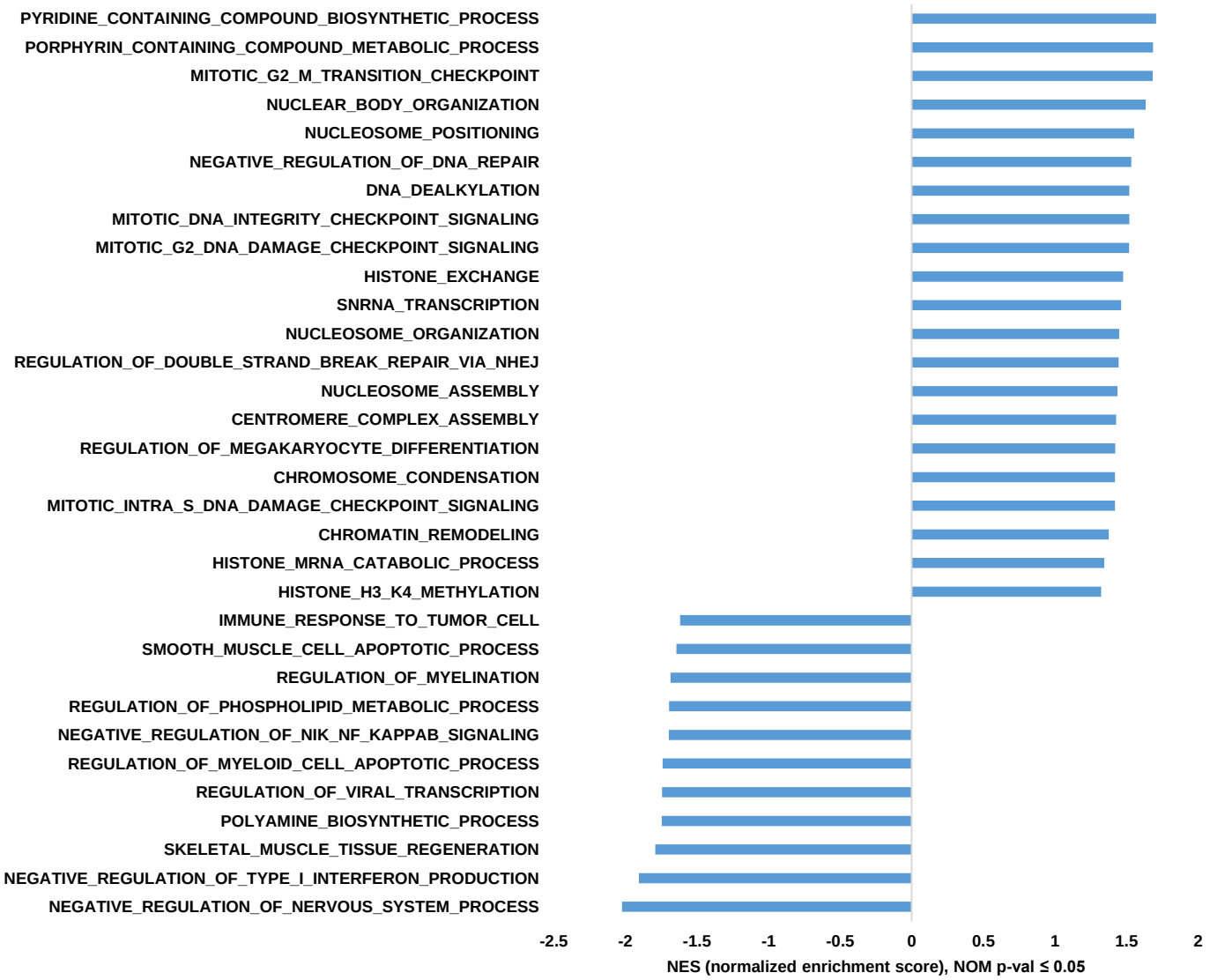

Figure 3

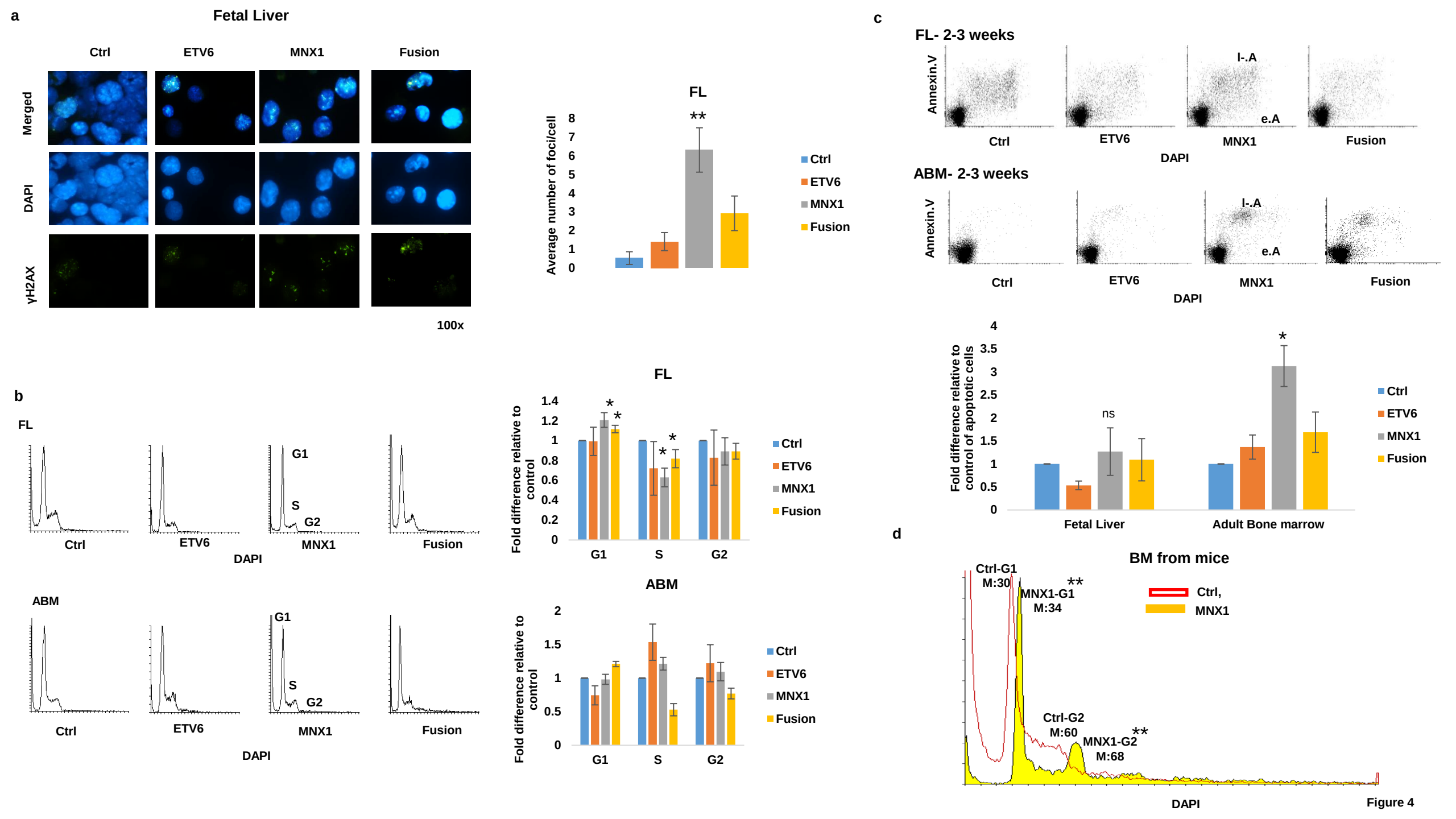
a
Fetal Liver
Ctrl
ETV6
MNX1
Fusion
Merged
DAPI
γH2AX
100x
FL
Average number of foci/cell
**
Ctrl
ETV6
MNX1
Fusion
b
FL
G1
S
G2
Ctrl
ETV6
MNX1
Fusion
DAPI
ABM
Fold difference relative to control
G1
S
G2
c
FL- 2-3 weeks
Annexin.V
l-.A
e.A
ABM- 2-3 weeks
Fold difference relative to control of apoptotic cells
ns
Fetal Liver
Adult Bone marrow
d
BM from mice
Ctrl-G1
M:30
MNX1-G1
M:34
Ctrl,
MNX1
Ctrl-G2
M:60
MNX1-G2
M:68
DAPI

Figure 4

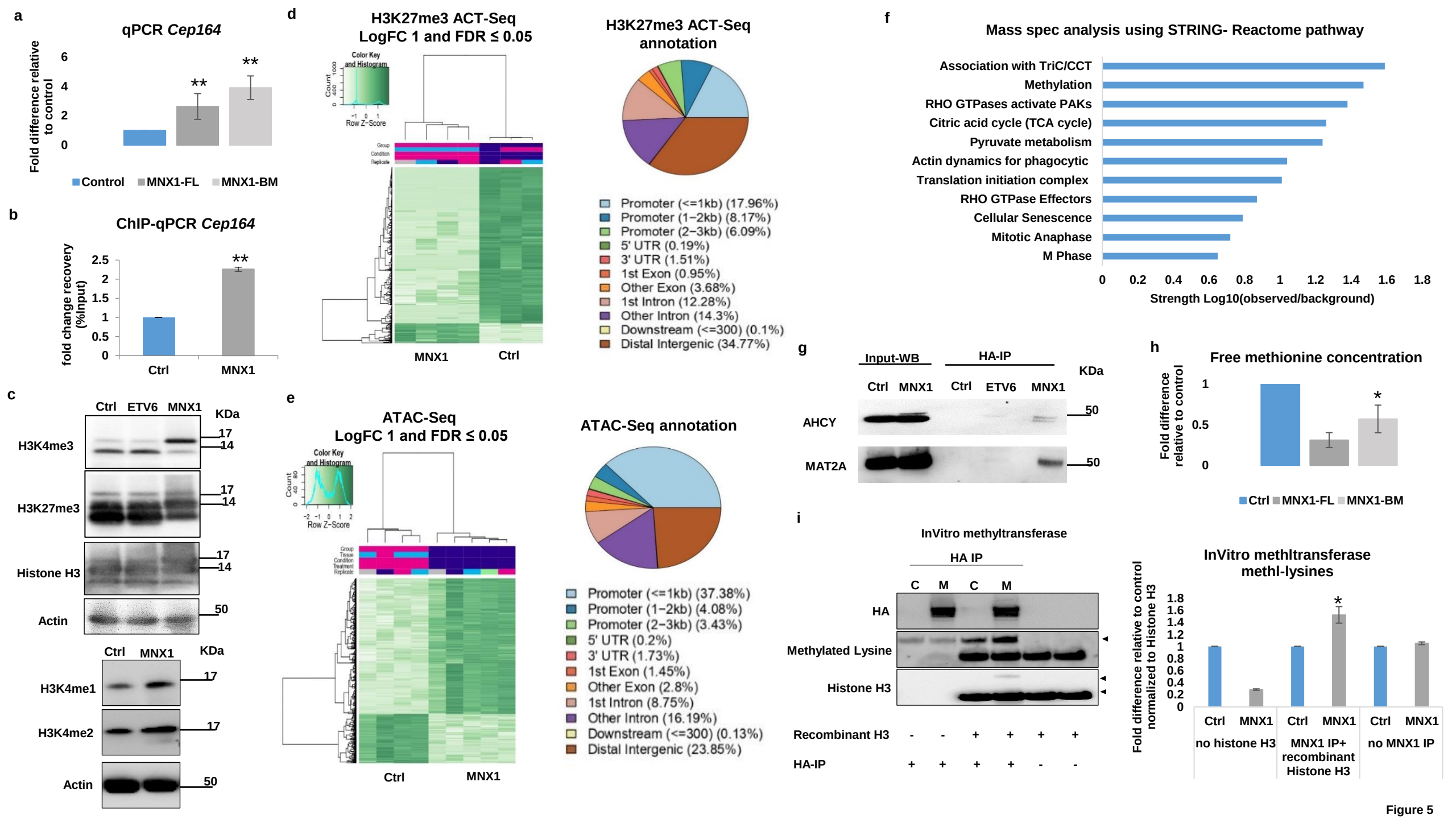
a
qPCR Cep164
Fold difference relative to control
Control
MNX1-FL
MNX1-BM
b
ChIP-qPCR Cep164
fold change recovery (%Input)
Ctrl
MNX1
c
Ctrl
ETV6
MNX1
KDa
H3K4me3
H3K27me3
Histone H3
Actin
H3K4me1
H3K4me2
d
H3K27me3 ACT-Seq
LogFC 1 and FDR ≤ 0.05
Color Key and Histogram
Row Z-Score
H3K27me3 ACT-Seq annotation
Promoter (<=1kb) (17.96%)
Promoter (1−2kb) (8.17%)
Promoter (2−3kb) (6.09%)
5' UTR (0.19%)
3' UTR (1.51%)
1st Exon (0.95%)
Other Exon (3.68%)
1st Intron (12.28%)
Other Intron (14.3%)
Downstream (<=300) (0.1%)
Distal Intergenic (34.77%)
e
ATAC-Seq
LogFC 1 and FDR ≤ 0.05
ATAC-Seq annotation
Promoter (<=1kb) (37.38%)
Promoter (1−2kb) (4.08%)
Promoter (2−3kb) (3.43%)
5' UTR (0.2%)
3' UTR (1.73%)
1st Exon (1.45%)
Other Exon (2.8%)
1st Intron (8.75%)
Other Intron (16.19%)
Downstream (<=300) (0.13%)
Distal Intergenic (23.85%)
f
Mass spec analysis using STRING- Reactome pathway
Association with TriC/CCT
Methylation
RHO GTPases activate PAKs
Citric acid cycle (TCA cycle)
Pyruvate metabolism
Actin dynamics for phagocytic
Translation initiation complex
RHO GTPase Effectors
Cellular Senescence
Mitotic Anaphase
M Phase
Strength Log10(observed/background)
g
Input-WB
HA-IP
AHCY
MAT2A
h
Free methionine concentration
Fold difference relative to control
i
InVitro methyltransferase
HA IP
HA
Methylated Lysine
Recombinant H3
HA-IP
InVitro methltransferase methl-lysines
Fold difference relative to control normalized to Histone H3
no histone H3
MNX1 IP+ recombinant Histone H3
no MNX1 IP

Figure 5

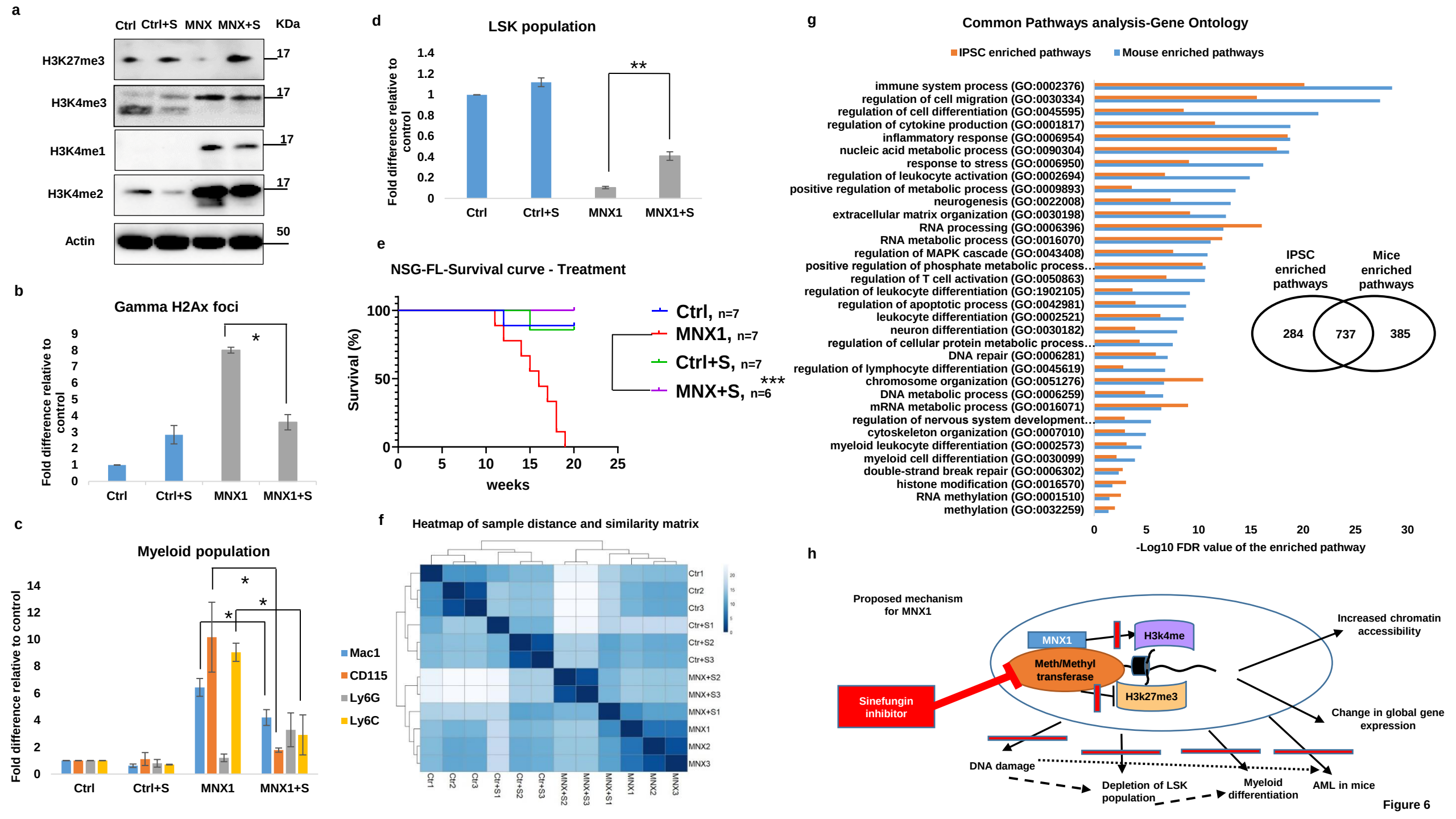
a
Ctrl Ctrl+S MNX MNX+S KDa
H3K27me3
H3K4me3
H3K4me1
H3K4me2
Actin
17
17
17
17
50
b
Gamma H2Ax foci
Fold difference relative to control
Ctrl
Ctrl+S
MNX1
MNX1+S
c
Myeloid population
Fold difference relative to control
Mac1
CD115
Ly6G
Ly6C
d
LSK population
Fold difference relative to control
Ctrl
Ctrl+S
MNX1
MNX1+S
e
NSG-FL-Survival curve - Treatment
Survival (%)
weeks
Ctrl, n=7
MNX1, n=7
Ctrl+S, n=7
MNX+S, n=6
f
Heatmap of sample distance and similarity matrix
g
Common Pathways analysis-Gene Ontology
IPSC enriched pathways
Mouse enriched pathways
immune system process (GO:0002376)
regulation of cell migration (GO:0030334)
regulation of cell differentiation (GO:0045595)
regulation of cytokine production (GO:0001817)
inflammatory response (GO:0006954)
nucleic acid metabolic process (GO:0090304)
response to stress (GO:0006950)
regulation of leukocyte activation (GO:0002694)
positive regulation of metabolic process (GO:0009893)
neurogenesis (GO:0022008)
extracellular matrix organization (GO:0030198)
RNA processing (GO:0006396)
RNA metabolic process (GO:0016070)
regulation of MAPK cascade (GO:0043408)
positive regulation of phosphate metabolic process...
regulation of T cell activation (GO:0050863)
regulation of leukocyte differentiation (GO:1902105)
regulation of apoptotic process (GO:0042981)
leukocyte differentiation (GO:0002521)
neuron differentiation (GO:0030182)
regulation of cellular protein metabolic process...
DNA repair (GO:0006281)
regulation of lymphocyte differentiation (GO:0045619)
chromosome organization (GO:0051276)
DNA metabolic process (GO:0006259)
mRNA metabolic process (GO:0016071)
regulation of nervous system development...
cytoskeleton organization (GO:0007010)
myeloid leukocyte differentiation (GO:0002573)
myeloid cell differentiation (GO:0030099)
double-strand break repair (GO:0006302)
histone modification (GO:0016570)
RNA methylation (GO:0001510)
methylation (GO:0032259)
-Log10 FDR value of the enriched pathway
IPSC enriched pathways
Mice enriched pathways
284
737
385
h
Proposed mechanism for MNX1
MNX1
H3k4me
Meth/Methyl transferase
H3k27me3
Sinefungin inhibitor
Increased chromatin accessibility
Change in global gene expression
DNA damage
Depletion of LSK population
Myeloid differentiation
AML in mice

Figure 6